

# Revisiting the Galactic Winds in M82 I: the recent starburst and launch of outflow in simulations

Tian-Rui Wang,<sup>1</sup> Weishan Zhu,<sup>1</sup>★ Xue-Fu Li,<sup>1</sup> Wen-Sheng Hong<sup>2</sup> and Long-Long Feng<sup>1</sup>

<sup>1</sup>*Department of Astronomy, Sun Yat-Sen University, No. 2 Daxue Road, Xiangzhou District, Zhuhai, 519082, China*

<sup>2</sup>*Department of Astronomy, School of Physics and Astronomy, and Shanghai Key Laboratory for Particle Physics and Cosmology, Shanghai Jiao Tong University, Shanghai 200240, People's Republic of China*

Accepted XXX. Received YYY; in original form ZZZ

## ABSTRACT

We revisit the launch of the galactic outflow in M82 through hydrodynamic simulations. Employing a sink-particle module, we self-consistently resolve the star formation and feedback processes, avoiding the reliance on various assumed models. We probe the effects of different stellar feedback mechanisms, gas return from star-forming clouds and gas disc mass on the starburst and outflow. Our simulations can generate a starburst that lasts  $\sim 25$  Myr, peaking at  $20\text{--}50\text{ M}_{\odot}\text{yr}^{-1}$ . However, the total stellar mass formed in the starburst often exceeds M82's estimated value. The outflow's launch occurs in two stages. Initially, continuous SNe explosions form small bubbles, merging into a super bubble foam composed of warm/hot gas and high-density cool filaments. After  $\sim 10$  Myr of SN injection, the super bubble breakout the disc, marking the second stage, which takes  $\sim 15$  Myr to develop a kpc-scale outflow. Our simulations reveal that cool filaments within the ISM can survive from the stellar feedback, then were entrained into the outflow and stretched to hundreds pc in length. While the mass loading factor of the well-developed outflow is comparable to M82, the cool gas mass outflow rate is often lower, and its velocity is slower than the estimated value in M82 by  $\sim 60\%$ . Warm and hot gas are  $\sim 25\%$  slower. SN feedback acts as the primary driver of the outflow, while gas return significantly influences the starburst and outflow. Other factors have moderate effects. To address the shortcoming in our results, enhanced SN feedback effect due to clustered SNe is likely necessary.

**Key words:** galaxies: starburst – galaxies: evolution – galaxies: ISM

## 1 INTRODUCTION

Since their initial discovery in M82 by Lynds & Sandage (1963), galactic winds and outflows have been observed in both nearby and at high redshift (e.g. McCarthy et al. 1987; Heckman et al. 1990; Martin 1999; Heckman et al. 2000; Rupke et al. 2005; Weiner et al. 2009; Martin et al. 2012; Arribas et al. 2014; Genzel et al. 2014; Heckman et al. 2015; Fluetsch et al. 2019; Keerthi Vasan et al. 2023; Perrotta et al. 2023; Xu et al. 2023a; Carniani et al. 2024; Weldon et al. 2024). Observations spanning multiple bands have revealed that galactic winds are complex, multi-phase structures that extend from a few parsecs to tens of kiloparsecs. These outflows contain a mixture of gas phases, including cold ( $T \lesssim 10^3$  K), cool ( $T \sim 10^3\text{--}2 \times 10^4$  K), warm ( $2 \times 10^4\text{ K} \lesssim T \lesssim 5 \times 10^5$  K), hot ( $5 \times 10^5 < T < 10^7$  K), and very hot ( $T > 10^7$  K) gaseous, and dust (for more details, see reviews by Veilleux et al. 2005, 2020; Heckman & Thompson 2017; Rupke 2018 and references therein). Observations, analytical models, and simulations have established that stellar feedback, including supernovae, stellar winds, radiation, and possibly cosmic rays, and active galactic nuclei (AGN) feedback can drive galactic-scale outflows, reproducing observed multi-phase structures (e.g., Chevalier & Clegg

1985; Strickland & Stevens 2000; Murray et al. 2005). Extensive research suggests that these outflows play a crucial role in the redistributing of the interstellar medium (ISM), regulating the efficiency of star formation and enriching the circumgalactic medium (CGM) and intergalactic medium (IGM) (Dekel & Silk 1986; Cole et al. 1994; Naab & Ostriker 2017). This work focuses on stellar feedback-driven outflows, widely considered to be the primary mechanism for suppressing star formation in low-mass galaxies.

Despite significant progress over the past six decades, many fundamental questions about galactic winds remain unanswered. Observationally, precisely measuring the key properties of outflows, including velocities, mass, momentum, and energy outflow rates, particularly for warm, cool, and cold phases, remains challenging (Heckman & Thompson 2017; Rupke 2018; Veilleux et al. 2020). Theoretically, while analytical models and simulations can explain hot winds, the mechanisms accelerating cool gas to hundreds of km/s remain uncertain. The roles of radiation pressure and cosmic rays in boosting galactic winds and accelerating warm and cool phases are also open questions (Heckman & Thompson 2017; Zhang 2018). Furthermore, simulations of galactic winds in galaxies with similar stellar and gas mass can yield divergent results due to variations in simulation setups, including SN feedback prescriptions, resolution, and initial ISM conditions.

★ E-mail: zhuwshan5@mail.sysu.edu.cn (WSZ)

A deeper understanding of how stellar feedback initiates galactic winds and the underlying processes driving their evolution is essential. Such knowledge will not only help interpret growing observational data but also solidify the modern  $\Lambda$ CDM paradigm of galaxy formation and evolution (e.g., [Naab & Ostriker 2017](#)). Within this framework, galactic winds are crucial for suppressing star formation in galaxies below the characteristic luminosity  $L_*$ , preventing overproduction of faint galaxies (e.g., [Dekel & Silk 1986](#); [Cole et al. 1994](#); [Somerville & Davé 2015](#)). Recent cosmological simulations of galaxy formation and evolution, such as Horizon-AGN ([Dubois et al. 2014](#)), EAGLE ([Schaye et al. 2015](#)), IllustrisTNG ([Pillepich et al. 2018](#)), Simba ([Davé et al. 2019](#)), have incorporated galactic winds and AGN feedback to successfully reproduce many observed galaxy properties. However, despite addressing similar physical processes, these simulations employ diverse sub-grid models for stellar feedback and galactic winds. EAGLE utilizes stochastic thermal heating from massive stars, Horizon-AGN adopts mechanical feedback ([Kaviraj et al. 2017](#)), and IllustrisTNG employs isotropic kinetic winds. Furthermore, the values of key parameters, including kinetic energy fraction, velocity, and mass outflow rate, vary significantly across these codes.

To gain a deeper understanding of galactic winds, a systematic theoretical investigation across multiple scales is necessary. On a parsec scale, detailed studies are required to explore the formation and lifetime of cold gas clumps and filaments in hot winds (e.g., [Cooper et al. 2009](#); [McCourt et al. 2015](#); [Scannapieco & Brüggén 2015](#); [Gronke & Oh 2018](#)), thermal instability in multi-phase winds, dust-gas coupling, and the efficiency of radiation pressure and cosmic rays, using both analytical models and simulations. Concurrently, global models and simulations spanning kpc scales are needed to examine the combined effects of these processes in realistic galaxy environments. Nearby galaxies with extensive observations, such as M82, provide ideal laboratories for testing these global simulations.

Numerous simulations of M82-like galaxies have been conducted over the past four decades. Early studies often employed one- and two-dimensional, axisymmetric simulations to investigate the development of galactic winds driven by nuclear starbursts in isothermal interstellar medium (e.g., [Tomisaka & Ikeuchi 1988](#); [Suchkov et al. 1994, 1996](#); [Tenorio-Tagle & Muñoz-Tuñón 1998](#); [Mac Low & Ferrara 1999](#); [Strickland & Stevens 2000](#); [Tenorio-Tagle et al. 2003](#); [Strickland & Heckman 2009](#)). These idealized simulations have validated the [Chevalier & Clegg \(1985\)](#) model in the adiabatic phase and demonstrated that the properties of the wind, such as dynamics, morphology, and X-ray emission, are influenced by factors such as the distribution of the interstellar medium, the ambient gaseous halo, and the distribution and clustering of young stars.

More recently, three-dimensional simulations (e.g., [Cooper et al. 2008](#); [Rodríguez-González et al. 2008](#); [Melioli et al. 2013](#)) have been employed to model M82's winds. [Cooper et al. \(2008\)](#) demonstrated that H- $\alpha$  filaments form from disk clouds entrained and stretched by the hot wind, emphasizing the role of the inhomogeneous disk in shaping the wind's filamentary structure. [Rodríguez-González et al. \(2008\)](#) and [Melioli et al. \(2013\)](#) highlighted the importance of radiative interactions between winds from super star clusters (SSCs), as well as the number, distribution, and buildup of SSCs, in developing H- $\alpha$  filaments. Very recently, [Schneider et al. \(2020\)](#) and [Schneider & Mao \(2024\)](#) conducted three-dimensional simulations of outflows driven by clustered supernova feedback in a large domain ( $\sim 20$  kpc) with high resolution ( $\sim 5$  pc). These simulations successfully produced multiphase outflows that closely resemble M82's outflow in many aspects.

However, most previous simulations of M82's winds have some

limitations due to oversimplified assumptions and factors. A critical issue is the unresolved nature of the recent starburst in the central disk region. Instead of self-consistently resolving the starburst, previous simulations often manually introduce star clusters with varying total masses ( $1$  to  $6 \times 10^8 M_\odot$ ) in different studies ([Cooper et al. 2008](#); [Rodríguez-González et al. 2008](#); [Melioli et al. 2013](#); [Schneider et al. 2020](#)), spatial distributions, and age distributions. Additionally, assumptions about M82's properties, such as its mass model and gas distribution, are often outdated. Recent observations have revealed discrepancies with earlier studies, particularly regarding the rotation curve ([Greco et al. 2012](#)) and gas distribution (e.g., [Leroy et al. 2015](#)), etc. Furthermore, the resolution and numerical methods employed in many previous simulations, including stellar evolution, radiative cooling, radiative pressure, and heating, can be further refined.

To enhance our understanding of galactic winds, we revisit M82's outflows using high-resolution three-dimensional hydrodynamic simulations that incorporate updated knowledge of M82, a more realistic representation of the recent nuclear starburst, and refined numerical treatments of relevant physical processes. This work, the first in a series, focuses on resolving the nuclear starburst and the subsequent launch of kpc-scale galactic outflows. Our second work ([Li et al. 2024](#)) delves into the development of multiphase outflows and the impact of various factors on their properties. This paper is organized as follows. Section 2 outlines our methodology. Section 3 presents the properties of the starburst in our simulations. The launch of kpc-scale multiphase outflows is described in Section 4. Section 5 discusses our findings, including comparisons with previous work and limitations. Finally, Section 6 summarizes our findings.

## 2 METHOD

Section 2.1 outlines our adopted mass model for M82. Sections 2.2 and 2.3 detail the initial conditions and star formation modules, respectively. Section 2.4 describes the implementation of various feedback mechanisms. Radiative cooling and heating processes are discussed in Section 2.5. Finally, Section 2.6 provides an overview of the simulations presented in this work.

### 2.1 Mass model of M82

Recent observational advances have provided more detailed estimates of the mass and distribution of baryonic matter, including stars and various gas phases. Furthermore, recent observations of the rotation curve suggest the presence of a dark matter halo, which was not considered in earlier studies. We construct a mass model for M82 that incorporates these latest observations. While significant uncertainties remain in the masses of gas and stars, we account for these by varying parameters in our models. Our mass models generally follow the approach of previous studies (e.g., [Strickland & Stevens 2000](#); [Cooper et al. 2008](#); [Melioli et al. 2013](#); [Schneider et al. 2020](#)). Our mass models mainly account for the contribution of a stellar disk, a gas disk, and a dark matter halo. The latter is not considered in earlier works such as [Strickland & Stevens \(2000\)](#); [Cooper et al. \(2008\)](#); [Melioli et al. \(2013\)](#), but is needed to reproduce the latest observed rotation curve of M82 in [Greco et al. \(2012\)](#).

We adopt a [Miyamoto & Nagai 1975](#) profile for the stellar disk, with a mass of, with a mass of  $3.3 \times 10^9 M_\odot$ , a scale length of 1200 pc, and a scale height of 200 pc. M82 also consists of a bulge with a mass of  $\sim 5.0 \times 10^8 M_\odot$  in the central 1 kpc region. A considerable fraction of stars in the bulge is likely formed in the recent star bursts, considering the spatial overlapping. Since this work

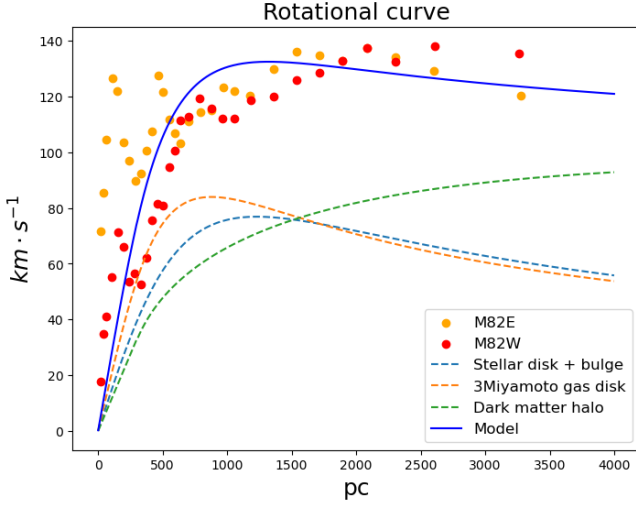


**Figure 1.** Observation results of the rotation curve provided by Greco et al. 2012 (red and yellow dots) and our model (blue solid line). The rotation curve contributed by the different components is shown as dashed lines.

focuses on simulating the recent starburst, we incorporate the bulge mass into the gas component, that is, the gas disk 2 in Table 1. The dark matter halo in our model follows a core-NFW profile with a mass of  $M_{\text{dmh}} \approx 6.0 \times 10^{10} M_{\odot}$ . The gas disk is modeled using a triple Miyamoto-Nagai profile similar to (Smith et al. 2015), with a mass of  $M_{\text{gd}} \approx 2.5, 3.0, 3.5 \times 10^9 M_{\odot}$ . We manage to determine the related parameters for each component so that the total rotation curve predicted by these components can reproduce the result in Greco et al. (2012), as Figure 1 shows. Detailed information about the mass model is provided in Appendix A.

## 2.2 Initial conditions in simulation

In our simulation, we first set up the gas distribution in each grid cell at the beginning of the simulation and then track the evolution of gas density and temperature, as well as star formation and feedback processes. The gravitational effect of the stellar disk and the dark matter halo is incorporated as a background field, a reasonable assumption for our 30 Myr simulation duration. The self-gravity of gas and newly formed stars is solved at each time step by the module in Athena++ (Stone et al. 2020).

The density profile of the gas disk component in the state of hydrostatic equilibrium under the galaxy gravity potential is given by

$$\rho(r, z) = \rho_0 \times \exp \left[ -\frac{\Phi_{\text{tot}}(r, z) - e^2 \Phi_{\text{tot}}(r, 0) - (1 - e^2) \Phi_{\text{tot}}(0, 0)}{c_s^2} \right], \quad (1)$$

where  $\rho_0$  is the central gas density, the rotational factor  $e$  reads as

$$e = e_{\text{rot}} \exp(-z/z_{\text{rot}}) \quad (2)$$

where  $e_{\text{rot}}$  in the above equation is chosen to be 0.92 for a thick disk. For the scale height  $z_{\text{rot}}$ , we choose a value of  $z_{\text{rot}} = 5$  kpc, following the literature (Suchkov et al. 1994; Strickland & Stevens 2000; Cooper et al. 2008). In addition to the gas disk, we also include a hot gas halo that follows a profile similar to that of Eqn. 1 but with a much smaller  $e_{\text{rot}}$ , which is consistent with previous studies (Strickland & Stevens 2000; Cooper et al. 2008). The parameters for the isothermal

**Table 1.** The initial central density,  $\rho_0$ , rotation factor,  $e_{\text{rot}}$ , and effective sound speed of the gas disk and halo. Gas disk 1 represents the dominate gas disk component. Gas disk 2 actually is used to mimic the potential of bulge, see text for more details.

Component	$\rho_0$ $\text{cm}^{-3}$	$e_{\text{rot}}$	$c_s$ $\text{cm} \cdot \text{s}^{-1}$
gas disk 1	190	0.92	$3.6 \times 10^6$
gas disk 2	70	0.5	$5.7 \times 10^6$
hot gas halo	$2.0\text{e-}3$	0.25	$3.0 \times 10^7$

disk and the hot gas halo are listed in Table 1. Note that  $c_s$  stands for the effective sound speed derived from the combined energy density of both the dynamic pressure provided by turbulence and the static pressure provided by internal energy, since the temperature of the gas disk quickly drops below  $10^4$  K where radiative cooling applies.

Observations reveal a turbulent interstellar medium (ISM) in M82, with non-thermal velocity dispersions of  $\sim 20 \text{ km s}^{-1}$  in molecular clouds (Westmoquette et al. 2012). Turbulence likely plays a significant role in both star formation and disk support. To account for this, we introduce turbulence into the initial gas disk. Unlike Cooper et al. (2008), who employed a static, inhomogeneous ISM with a lognormal probability density function, we perturb the velocity field using an energy spectrum function, given by

$$E_k(k) \propto k^{-p}, \quad (3)$$

and

$$\langle (\delta \mathbf{u}(r))^2 \rangle \propto r^{p-1}. \quad (4)$$

For typical Kolmogorov turbulence,  $p = \frac{5}{3}$ . However, turbulence in the ISM is generally supersonic (e.g. Elmegreen & Scalo 2004; Federrath et al. 2010a), with  $p$  closer to 2 (e.g. Boldyrev 2002; Federrath 2013). Given the mean velocity dispersion reported by Westmoquette et al. (2012), the ISM in the star-forming region of M82 is in a supersonic turbulent state. We initialize the gas velocity field as a superposition of rotational and turbulent components. This gas distribution is then evolved without cooling or feedback for 2.5 Myr to generate an inhomogeneous disk, which serves as the initial condition for our simulations.

## 2.3 Star formation

Previous simulations of M82's galactic winds often rely on prescribed star formation histories, such as instantaneous starbursts or constant star formation rates. Additionally, SN feedback has been injected into a thin disk plane (Strickland & Stevens 2000; Cooper et al. 2008), or a central 1 kpc spherical region based on assumed star cluster distributions (e.g., Melioli et al. 2013; Schneider et al. 2020; Schneider & Mao 2024). A key goal of our work is to more self-consistently model the recent starburst in M82's nuclear region and its associated feedback. To this end, both the star formation process and how they couple with the surrounding ISM are solved explicitly in our simulation.

Newly born stars are embedded in molecular clouds and are usually surrounded by overdense ISM. Recent simulations of dwarf galaxies, which resolve star formation down to the scale of molecular clouds, have employed various approaches to capture star formation process. For dwarf galaxies with masses of  $10^7 - 10^8 M_{\odot}$  and relatively low SFR, a star-by-star formation recipe (Gutcke et al. 2021), is effective when sub-parsec resolution is achieved. However, for galaxy-scale

simulations with coarser resolution (several parsecs or larger), a sink particle approach is more practical. This approach involves creating sink particles with masses exceeding that of a single star in high-density regions, allowing them to accrete mass from surrounding gas cells until they meet the criteria for spawning star particles, each representing a cluster of stars (e.g., Bate et al. 1995; Krumholz et al. 2004; Jappsen et al. 2005; Federrath et al. 2010b; Gong & Ostriker 2012; Gatto et al. 2016; Howard et al. 2016). We adopt a sink particle model based on the methods of Federrath et al. (2010b) and Howard et al. (2016) to solve the star formation process in our work.

We have implemented a sink particle solver within the Athena++ code (Stone et al. 2020) to handle star formation and evolution. At each time step, gas cells are inspected to determine if they meet the following criteria for forming a sink particle:

- (i) Jean’s instability: The gas cell must be gravitationally unstable.
- (ii) does not overlap with existing sink/star particle.
- (iii) convergent gas flow.
- (iv) located at the center of a dense gas clump.

These criteria are commonly used for sink particle implementations in mesh-based fluid dynamic solvers (e.g. Krumholz et al. 2004; Federrath et al. 2010b; Gong & Ostriker 2012). The criterion requiring the cell to be gravitationally bound has also been adopted in many studies. However, some studies indicate that stars can form in areas that are not gravitationally bound, such as the fast-expanding shell of an SNR bubble or a wind bubble (Cantat-Gaudin et al. 2018; Deharveng et al. 2009) or high-velocity fragments in the outflow area (Maiolino et al. 2017). To account for these scenarios, we relax the gravitational bound criterion in our simulations. The following subsections detail these criteria and the star formation process from sink particles.

### 2.3.1 Jean’s instability

A fundamental requirement for star formation is Jeans instability. In a mesh-based hydrodynamical code, this translates to a density threshold, as proposed by Truelove et al. (1997):

$$\rho_{th} = \frac{\pi}{16} \frac{c_s^2}{G\Delta x^2}, \quad (5)$$

where  $c_s$  is the local sound speed and  $\Delta x$  is the cell size. However, as noted by Federrath et al. (2010b), Truelove’s criterion is only applicable to regions undergoing free-fall collapse. To identify such regions, further analysis is necessary, as detailed in the following subsections.

### 2.3.2 Distance check

Even if gas clouds near a newly formed star cluster meet the density threshold for star formation, they can be disrupted by photoionization heating and radiative pressure from massive stars. In M82, star clusters are often embedded in molecular clouds with optical depths of up to  $\tau \sim 10$ . In such environments, radiative pressure may be comparable to supernovae in terms of momentum injection (Agertz et al. 2012). Combined with stellar winds, these early feedback processes can suppress star formation in neighboring regions. To account for this, we assign each sink particle a control volume that should not overlap with those of existing sink or star particles. The side length of these cubic control volumes is set to three times the grid cell size.

### 2.3.3 Convergent flow

To confirm that a candidate cell is undergoing free-fall collapse, we check for convergent gas flow. This requires that the divergence of the velocity field,  $\nabla \cdot \mathbf{v} < 0$ , is negative in the central cell of the control volume (Gong & Ostriker 2012).

### 2.3.4 Gravitational potential minimum

A sink particle is created in a candidate cell only if it corresponds to a local minimum of the gravitational potential (Federrath et al. 2010b),  $\Phi$ . In practice, we consider only the gravitational potential of the gas,  $\Phi_{gas}$ , when examining this criterion. Neglecting the background potential from the stellar disk and dark matter halo prevents the sink particle from being placed away from the densest region of the gas clump.

### 2.3.5 Gas accretion and star formation

Several methods exist for calculating gas accretion onto sink particles. Krumholz et al. (2004) categorize accretion into three scenarios based on the relative importance of pressure and gravity, as determined by the particle’s Bondi-Hoyle radius, and employ different accretion models accordingly. Gong & Ostriker (2012) introduce ‘ghost’ zones around particles and calculate accretion rates based on the flux at the zone boundaries. In our work, we adopt a simpler approach similar to Federrath et al. (2010b). Once a sink particle forms, gas accretion begins immediately. Grid cells within the control volume are continuously monitored, and any gas exceeding the density threshold  $\rho_{th}$  is directly accreted by the sink particle. The mass accretion rate of a sink particle at each time step is given by:

$$\Delta M = \sum (\min(\rho(i, j, k) - \rho_{th}(i, j, k), 0) \Delta V(i, j, k), \quad (6)$$

where the summation is taken over all the gas cells within the control volume of this sink particle. Such an implementation of gas accretion enforces Truelove’s stability criterion, as well as the conservation of mass. Furthermore, this scheme is reasonable because the Bondi-Hoyle radius (Bondi 1952),

$$r_{BH} = \frac{GM}{v^2 + c_s^2} \quad (7)$$

for a molecular cloud with a mass around  $10^4 \sim 10^5 M_\odot$  and a sound speed of  $\sim 1 \text{ km} \cdot \text{s}^{-1}$  and is larger than the resolution of the most refined grids in our simulation. The inflow toward a sink particle is therefore supersonic, making the specific choice of accretion rate proposed by Krumholz et al. (2004) irrelevant. In addition to mass conservation, momentum and metal mass are also conserved during accretion. The sink particle’s velocity is updated at each timestep using momentum conservation, and the accreted gas’s metallicity is assigned as the initial metallicity for newly formed stars.

We employ a widely used method to convert the gas accreted to sink particles into stellar mass at a rate of 20% per free-fall time. This conversion rate ensures that the surface star formation rate scales with density as  $\rho^{1.5}$ , consistent with the Kennicutt-Schmidt law (Gutcke et al. 2021). The star formation rate for a sink particle at time  $t$  is given by:

$$\dot{M}_*(t) = \frac{M_{gas}(t)}{t_{SF}}, \quad (8)$$

where  $M_{gas}(t)$  is the gas mass stored in this sink particle and

$$t_{SF} = \frac{1}{0.2} t_{ff} = \frac{1}{0.2} \sqrt{\frac{3\pi}{32G\rho}}. \quad (9)$$



During our simulation, the star formation time scale  $t_{SF}$  will be updated after accretion at each time step. Based on newly updated  $t_{SF}$ , a fraction of the gas stored in the reservoir will be converted to stellar mass following Equation 8 within each time step, and then the stellar mass of each sink particle is updated. In this way, a sink particle represents both a gravitationally bound star-forming gas clump and the embedded stars within it (Howard et al. 2016).

Initially, the stellar mass within a star-forming gas clump grows gradually. However, once the stellar mass in a gas clump exceeds some critical value, the gas accretion would cease due to feedback from newly born stars. In our simulation, if the stellar mass in a sink particle exceeds a threshold value of  $M_{cny}$ , it will stop accreting gas and be reclassified as a star particle. The mass of star clusters in M82 can vary from  $1000 M_{\odot}$  to as high as  $10^6 M_{\odot}$ . Observations show that the median mass of super star clusters (SSCs) in M82 is around  $10^{4.12} M_{\odot}$  and the median radius is around 4.26 pc (Cuevas Otaola et al. (2020)).

In our simulation, the radius of the control volume of a sink particle,  $R_{cv}$ , is  $\sim 1.5$  times the size of the nearby grid. Since sink particles can form in regions with varying resolutions, their control volumes and the corresponding Jeans masses  $M_J$  can differ. A fixed mass threshold,  $M_{cny}$ , could lead to inconsistent distribution of stellar mass fraction, i.e. the ratio of stellar mass to the total mass in a star particle, across regions with different resolutions. To ensure a consistent distribution of the stellar mass fraction, we adopt a variable  $M_{cny}$ . Based on the assumption that a) the total accreted mass is proportional to Jeans mass, b) sink particles of different sizes have a constant temperature, and c) the stellar mass fraction is independent of the particle mass, we derive  $M_{cny} \propto M_J \propto R_{cv}$ . In our simulation, we adopt  $M_{cny} = 5.0 \times 10^4 M_{\odot}$  for the finest grids with  $dx = 4.0 pc$ ,  $M_{cny} = 1.0 \times 10^5 M_{\odot}$  for  $dx = 8.0 pc$ , etc.

## 2.4 Feedback

Stellar feedback serves as the main driving force for the launch of the galactic outflow. Traditionally, the primary feedback mechanism considered in similar studies is the core-collapse SNe, which has been proven capable of launching galaxy-scale outflow in M82 (e.g. Strickland & Stevens 2000; Cooper et al. 2008; Schneider et al. 2020). However, recent studies show that radiation feedback and stellar wind may play crucial roles in manipulating the effect of SNe feedback (Dale et al. 2014; Chevance et al. 2020). These early feedback processes may significantly lower the SFR and prevent the clustering of star formation. Some previous work suggests that efficient X-ray and extreme ultraviolet (EUV) radiation are capable of removing important coolants through photoionization, leading directly to the reduction of the accretion rate and SFR (e.g. Cantalupo 2009). Furthermore, stellar wind can create cavities and channels of ionized gas before the first SNe, mitigating the resistance an expanding SNR may meet. In this study, we consider three major feedback processes: radiation, stellar wind, and core-collapse SNe. We will examine how these mechanisms affect the starburst activity and the launch of outflow in M82. The effects of Type Ia SNe are ignored because our simulations last for 30 Myr, in which period type Ia SNe should have a limited effect in contrast to the core-collapse SNe. In our simulations, the stellar mass of a single star particle is equivalent to a medium-sized star cluster. Therefore, it can continuously produce stellar wind and radiation feedback and it will launch several individual SNe throughout its lifetime.

On the other hand, not all the gas in sink/star particles (GMCs) will convert to stars. Stellar feedback can disperse a great amount of the remaining gas in GMCs, causing a considerable amount of gas to

return to the diffuse ISM. Studies indicate that up to 80% of the mass of star-forming gas clumps will return back to the ambient diffuse ISM within the time scale of  $5 \sim 15$  Myr, equivalent to several to ten times of the newly born stellar mass (e.g., Dale et al. 2014; Kim et al. 2018; Li et al. 2019; Fujii et al. 2021). This process of gas return can have substantial effects on the initiation and development of outflows. The detailed implementations of gas return and the three stellar feedback processes mentioned above are also introduced in this subsection, and their effects will be presented in later sections.

### 2.4.1 Gas return from sink particle

Most previous studies that adopted a sink particle-based star formation scheme have not included any returning mechanism for the remaining gas in sink particles. Some of these studies may assume that all the gas in sink particles will fully convert to stars (e.g. Wang et al. 2010; Padoan & Nordlund 2011; Gong & Ostriker 2012; Kim et al. 2018), which is valid only if the resolution can reach 0.1 parsec or higher. However, this treatment may overestimate the star formation efficiency in simulations with a resolution coarser than the size of the cores of GMCs. Meanwhile, other simulation studies on the evolution of GMC and ultra-faint dwarf galaxies believe that most unresolved gas in sink particles remains gravitationally bound to the cluster formed in GMC over a long time scale (Dale et al. 2014; Howard et al. 2016). Therefore, gas is stored in sink particles in these studies. However, in simulations with a relatively coarser resolution or with a long simulation time, such a treatment would cause a great fraction of the gas to be locked up in particles (Truelove et al. 1997; Hu et al. 2017), leading to an underestimation of the star formation efficiency. Overall, both approaches mentioned above have their own limitations. Recent studies indicate that early pre-supernovae feedback processes (i.e. stellar wind, radiation feedback) are capable of destroying the cloud and accelerating a great portion of the remaining gas to a gravitationally unbound state within  $2 \sim 15$  Myr, in which the returning fraction may depend on the properties of the gas clumps (e.g., Kim et al. 2018; Li et al. 2019).

In our simulation, we use a simplified model to account for the dispersal of gas remaining in the sink/star particles. In the default run, we assume that all the remaining gas in the particles can eventually escape from their hosts. For comparison, we have also adopted two different setups in other runs, one with a gas return fraction of 50%, the other with the gas return fully disabled. The return of the remaining gas in a particle begins 2.0 Myr after star formation, based on previous simulations (e.g. Dale et al. 2014; Kim et al. 2018; Li et al. 2019; Fukushima & Yajima 2021). Moreover, the gas stored in a particle will return to the surrounding grid cells as an exponential function of time on a time scale  $\tau_{rin}$

$$\dot{M}_{gas} = -\frac{M_{gas}}{\tau_{rin}}. \quad (10)$$

Here in our simulation, a time scale of  $\tau_{rin} = 5.0 Myr$  is adopted. At each time step, gas leaked from a particle is injected into grid cells within the particle's control volume with an initial velocity equal to that of the host particle, and subsequently accelerated by stellar winds and radiation pressure applied to the same region.

### 2.4.2 Radiation

Multiple researches have shown that radiation pressure and photoionization dominate over gas pressure in the central region of molecular clouds, acting as the main mechanisms for cloud destruction and disrupting star formation (Ceverino et al. 2013; Sales et al. 2013).

More recently, radiation feedback has been proven capable of removing gas from the center of a molecular cloud and carving channels into the outer region, allowing supernova remnants to pass through without much resistance (Dale et al. 2014; Fujii et al. 2021). Emerick et al. (2018) shows that these two mechanisms can play a catalytic role in the launch of galactic outflow in a low-mass dwarf galaxy. To investigate the effect of radiation, we incorporate both radiation pressure and radiation heating feedback in our simulation. Note that photoionization is not explicitly included in our simulation. Instead, we employ photoelectric heating in our cooling/heating source term for the following reasons: 1) resolving the detailed chemical evolution is not the main intention of this work, and 2) most of the gas in M82 remains neutral throughout the starburst, while ionized gas in the dense area will recombine quickly. From a statistical point of view, photoionization can be treated as a heating term. In our simulation, only UV radiation is considered, as it carries the most energy and momentum at the early age of a starburst galaxy. We use two separate modules to account for the effect of the photoheating and radiation pressure separately, both of which will be described in this section.

For photoelectric heating, we use equation 1 in Wolfire et al. (1995) to calculate the heating rate. This method has been implemented into the GRACKLE library and integrated with heating and cooling routines. To compute photoelectric heating, the intensity of the interstellar radiation field must first be determined. To this end, we use an approach different from the optically thin assumption, considering that most parts of the M82's gas disk, especially the star forming clumps and SNR bubble shells, are opaque to UV radiation (Murray et al. 2009). Thompson et al. (2008) suggested that the characteristic opacity of UV radiation is  $\kappa_{UV} \sim 10^3 \text{ cm}^2 \cdot \text{g}^{-1}$  in the neutral gas. The two-temperature Planck mean opacity calculated from OPTAB (Hirose et al. 2021) also shows that for a typical OB star with an effective surface temperature of more than  $10^5 \text{ K}$  surrounded by ambient gas with a temperature ranging from 10 to 20000 K, the opacity can be as high as  $10^2 \sim 10^3 \text{ cm}^2 \cdot \text{g}^{-1}$ . In such an environment, the inverse-square law could overestimate the intensity of the UV radiation field by a few orders of magnitude in a region far away from the UV source. To correct for this effect, we instead use a modified inverse-square law to estimate the intensity of the radiation field. More specifically, the UV flux distribution is obtained by solving the point-source divergence equation with absorption under spherical symmetry as follows.

$$\nabla F = -F\kappa\rho, \quad (11)$$

where  $\kappa$  is the opacity of the medium. The radial fraction of the equation gives

$$\frac{1}{r^2} \frac{\partial r^2 F}{\partial r} = -F\kappa\rho. \quad (12)$$

Consequently, the profile of the radiation field resulting from a point source is

$$F_r = F_0 \frac{1}{r^2} e^{-\kappa\rho r}, \quad (13)$$

or alternatively

$$F_r = F_0 \frac{1}{r^2} e^{-r/\lambda_{UV}}, \quad (14)$$

where  $\lambda_{UV} = \kappa\rho$  is the local UV attenuation length. In practice, to reduce computational cost,  $\lambda_{UV}$  is calculated using the average density in each mesh block ( $8 \times 8 \times 8$  gas cells around the star particle). At each time step of the simulation, the UV radiation intensity at a gas cell is calculated by the summation of UV radiation fields produced

by star particles within the distance of 5 times  $\lambda_{UV}$ . A maximum distance of 200 pc is also enforced when performing the summation.

On the other hand, radiation pressure is implemented as a momentum source. Sales et al. (2013) suggested that the radiation pressure is capable of accelerating the gas to a velocity up to  $50 \sim 100 \text{ km s}^{-1}$  especially in high-density regions with  $n_H > 1000 \text{ cm}^{-3}$ , where the recombination time is short. Given the very high infrared (IR) opacity in molecular clouds, IR photons reradiated from dust grains will scatter multiple times before escaping, providing an extra boost to radiation pressure (Agertz et al. 2012; Sales et al. 2013). In order to resolve the radiation pressure from multiple sources while keeping a reasonable computation cost, we reuse the UV field derived previously in equation 14 to calculate the local volumetric UV absorption rate

$$I = F \cdot \kappa \cdot \rho \quad (15)$$

The volumetric momentum injection rate of radiation pressure is then given by

$$\dot{P}_{rad} = (\eta_1 + \eta_2 \tau_{IR}) \frac{I}{c}. \quad (16)$$

where  $\eta_1$  and  $\eta_2$  adopt the value of 1.0 in areas that are fully opaque to UV and IR. Optical depth  $\tau$  takes the simplified form of

$$\tau = \kappa \cdot \rho \cdot L \quad (17)$$

where  $L$  is the length of the transmission path of the light. The IR optical depth  $\tau_{IR}$  in M82's star cluster is assumed to be  $10 \sim 100$  based on the observed densities (Agertz et al. 2012), therefore IR may be the dominant term in radiation pressure. In the calculation of optical depth, we use a similar approach to that in the calculation of self-shielding in GRACKLE (Smith et al. 2016), we use the local Jeans length  $R_J$  as the radius of the host clump within which the grid cell resides, therefore

$$\tau = \kappa \cdot \rho \cdot R_J \quad (18)$$

Finally, we compute the radiation pressure exerted on the boundary of a grid cell by dividing the volumetric momentum injection rate by the surface area of the grid cell. Since we treat radiation pressure as a momentum source term, the effect of radiation pressure is then

$$\frac{dP}{dt} = -\nabla P_{Radiation} \quad (19)$$

#### 2.4.3 Stellar Wind

In addition to radiation and SNe, the stellar wind is a non-negligible source of feedback, which could be comparable to that of SNe under certain circumstances (Agertz et al. 2012). We adopt a metallicity-dependent model proposed by Vink & Sander (2021) to calculate the stellar wind's mass loss rate and final velocity.

#### 2.4.4 Core-collapse SNe

Conventionally, stars within the zero-age main sequence mass range of  $8 \sim 30 M_\odot$  are thought to end their life through the outbreak of core-collapse supernovae (CCSN). Most previous models use a fixed thermal energy injection value of  $10^{51} \text{ erg}$ . However, recent studies indicate that the energy and mass of the ejecta as well as the composition of the ejecta depend on certain parameters, especially the ZAMS mass of the progenitor. In our study, we mainly follow the work of Gutcke et al. (2021). We divide the total mass of each star particle (star cluster) into multiple ZAMS stars according to a Kroupa (2002) IMF. In practice, instead of creating many refined

**Table 2.** List of all the simulations performed, the first and second columns are the name and mass of gas disc, respectively. The third, fourth and fifth column indicate the setting of supernovae, stellar winds and radiation feedback, respectively. The sixth and seventh columns indicate the gas return fraction and initial gas metallicity respectively (see section 2.6 for more details).

Simulation name	$M_{\text{gd}}$	supernovae	Stellar Wind	Radiation	Gas Return	$Z_{\text{ini}}$
FD	$3.0 \times 10^9 M_{\odot}$	vSN(S16)	Yes	Yes	100%	$0.02 Z_{\odot}$
fSN	$3.0 \times 10^9 M_{\odot}$	$E_{\text{SN}} = 10^{51} \text{ erg}$	Yes	Yes	100%	$0.02 Z_{\odot}$
nSN	$3.0 \times 10^9 M_{\odot}$	No	Yes	Yes	100%	$0.02 Z_{\odot}$
nWind	$3.0 \times 10^9 M_{\odot}$	vSN(S16)	No	Yes	100%	$0.02 Z_{\odot}$
nRad	$3.0 \times 10^9 M_{\odot}$	vSN(S16)	Yes	No	100%	$0.02 Z_{\odot}$
nFB	$3.0 \times 10^9 M_{\odot}$	No	NO	No	100%	$0.02 Z_{\odot}$
GL00	$3.0 \times 10^9 M_{\odot}$	vSN(S16)	Yes	Yes	0%	$0.02 Z_{\odot}$
GL05	$3.0 \times 10^9 M_{\odot}$	vSN(S16)	Yes	Yes	50%	$0.02 Z_{\odot}$
M25	$2.5 \times 10^9 M_{\odot}$	vSN(S16)	Yes	Yes	100%	$0.02 Z_{\odot}$
M35	$3.5 \times 10^9 M_{\odot}$	vSN(S16)	Yes	Yes	100%	$0.02 Z_{\odot}$
Z01	$3.0 \times 10^9 M_{\odot}$	vSN(S16)	Yes	Yes	100%	$0.1 Z_{\odot}$
Z05	$3.0 \times 10^9 M_{\odot}$	vSN(S16)	Yes	Yes	100%	$0.5 Z_{\odot}$

small particles, we store a list of individual virtual stars' information, including mass and expected lifetime, for each star particle (star cluster). At each time step, we update the age of virtual stars and loop over the lists to locate all the massive stars that have exceeded their expected lifetime and then trigger either a CCSN or failed SN for each such virtual star. The injected energy, ejecta mass, and metal of each SN (failed SN) are then calculated from the Sukhbold et al. (2015) CCSN model accordingly. Stellar wind and UV radiation before the outbreak of CCSN have already cleared the path for SNe Dale et al. (2014). Therefore, we directly inject 100% of SNe's mass, metal, and energy output, together with the much enhanced stellar wind produced in the last few years of the pre-supernova stage (Das & Ray 2017), into grid cells within the control volume at the very end of their lifetime.

The lifetime of massive stars is calculated using a scheme similar to that of Gutcke et al. (2021), which involves linearly interpolating the table provided by Portinari et al. (1998) with an assumed metallicity equals to the initial gas metallicity, i.e.,  $Z = 0.02 Z_{\odot}$  for most runs. This model has been proven robust with small discrepancies compared to other stellar lifetime models such as Schaller et al. (1992) and Paxton et al. (2010). Note that not all stars with a ZAMS mass above  $8 M_{\odot}$  will end their lives as CCSN. A noticeable fraction of OB stars may collapse directly to form black holes during the core collapse, which is commonly referred to as failed SNe (Woosley & Weaver 1986; MacFadyen & Woosley 1999). Failed SNe often release considerably less energy, typically on the order of  $10^{49}$  erg, and result in a much smaller amount of mass return (e.g. Sukhbold et al. 2015). In our simulation, we apply the same mass and energy injection scheme for CCSN to these failed SNe, but with their mass, metal, and energy injection rates inferred from the Sukhbold et al. (2015) model.

Apart from the variable SNe model from Sukhbold et al. (2015), we have also adopted the widely used fixed energy ( $E_{\text{SN}} = 10^{51} \text{ erg}$ ) SNe model in run fSN, and compare the effect of the two different setups in the following sections.

## 2.5 radiative cooling and heating

Radiative cooling and heating play an important role in the evolution of ISM. In our simulation, we use GRACKLE (Smith et al. 2016), an

open-source chemistry and cooling library, to solve radiative cooling and heating. GRACKLE provides primordial and dust chemistry calculations, as well as tabulated metallicity-dependent cooling functions with and without self-shielding. Our work adopts a simplified chemistry network that accounts only for gas and metal; a tabulated ionization collisional equilibrium cooling function calculated from CLOUDY is used.

The cooling rate of the gas highly depends on the metallicity. For a star-forming gas cloud with constant feedback and metal enrichment, the metallicity can vary from the initial value of  $0.02 Z_{\odot}$  to as high as  $20 Z_{\odot}$ , causing the cooling rate to vary by an order of magnitude. This variation in the cooling rate could significantly affect the evolution of molecular clouds, the HII region, and the multiphase outflow. In order to obtain a more accurate result, we use a passive scalar as the tracer for metal elements in the ISM. Moreover, we include the SNe metal enrichment based on the isotope yield provided in the work of Sukhbold et al. (2015). Therefore, we can trace the detailed evolution of the metal elements in the ISM and calculate an accurate cooling function accordingly.

The gas disk of M82 is a highly gas-rich and dust-rich environment, where the optical-thin assumption may fail due to the large opacity in some regions. Previous studies argue that self-shielding can significantly reduce the cooling rate by an order of magnitude in cool to warm regions with relatively low density ( $\sim 1 \text{ cm}^{-3}$ ), which is enough for the radiation feedback to become significant to support the clouds from collapsing (Emerick et al. 2019). In our simulation, the self-shielding option provided by GRACKLE is turned on, in which the self-shielding of both HI and HeI from the UV background is included. The detailed derivation of the tabulated self-shielding cooling function in GRACKLE is described in the work of Smith et al. (2016) and Rahmati et al. (2012).

We also include photoelectric heating provided by GRACKLE in our simulation, detailed setup has been described in Section 2.4.2. Many previous simulations incorporate a delay cooling method, disabling radiation cooling around star clusters for a period of time, therefore ensuring that the SNR bubbles expand to the Sedov stage without losing much of their energy in the free expansion stage and increasing the effect of hot gas (e.g. Agertz et al. 2012). However, with UV radiation heating included, star clusters can efficiently ionize the



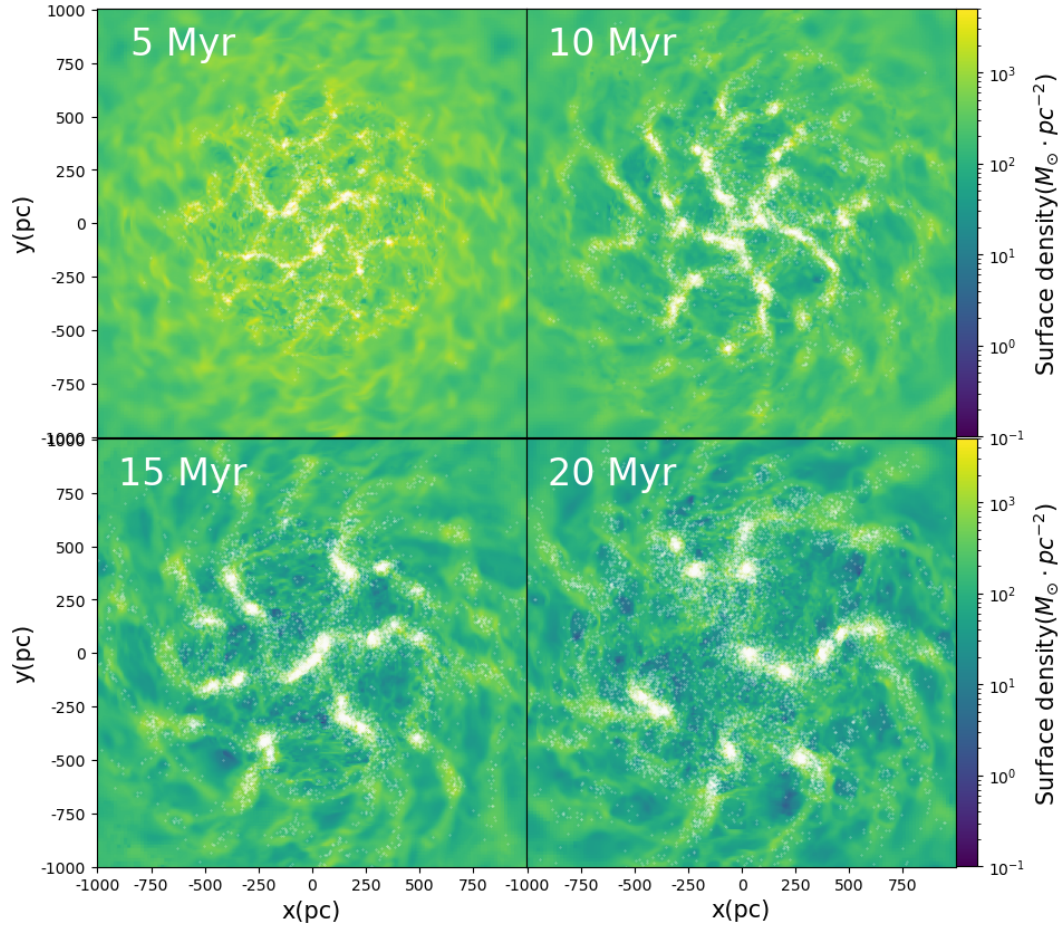


**Figure 2.** Face on view of the distribution of star particles (white dots) in the gas disc in the FD simulation, along with the projected gas density. This image shows how star particles are coupled with high-density clumps. The two lower images reveal how super bubbles are centered around clustered particles.

gas within a Strömgren radius  $r_S$ .

$$r_S = \left( \frac{3}{4\pi} \cdot \frac{N_{\text{ion}}}{n_H^2} \right)^{1/3} \quad (20)$$

in which  $N_{\text{ion}}$  is the number of H ionizing photons produced by the OB stars in the star cluster. We note that in a typical SSC in M82, the Strömgren radius can reach  $5 \sim 20$  pc in dense areas with  $n_H \sim 1000 \text{ cm}^{-3}$ , enough for the SNR to expand while conserving most of its energy. Overall, using photoelectric heating instead of delay gas cooling around star clusters provides a more sophisticated account for the mechanisms involved in the launch of the SNR bubbles while avoiding the introduction of artifacts.

## 2.6 Simulations

Our simulations were performed with the state-of-the-art grid-based MHD code Athena++ (Stone et al. 2020). We used the multi-grid self-gravity solver module developed by Kenko Tomida to solve the self-gravity hydrodynamic equations. We also used static mesh refinement (SMR) to refine the cells in the central starburst region to up to 4 pc resolution. The detailed setups of the simulations that we performed are listed in Table 2.

## 3 STARBURST IN OUR SIMULATIONS

Our simulations can generate a starburst in the central region of the gas disc. In this section, we report the features of the starburst and the stars formed. We begin with the star formation history and efficiency, and then probe the properties of star clusters.

### 3.1 star formation history and efficiency

M82 has undergone multiple starburst events throughout its history (Divakara Mayya & Carrasco 2009). The majority of stars in the stellar disk are between 300 Myr and 1 Gyr. The recent starburst, which occurred within the past 15 ~ 50 Myr in the nuclear region (within  $r < 625$  pc), is responsible for the current galactic outflow. Some studies suggest that this recent starburst comprised two distinct events (Rieke et al. 1993; Schreiber et al. 2003), with a major burst peaking around 8 ~ 15 Myr ago and having a peak SFR of  $160 \text{ M}_\odot \cdot \text{yr}^{-1}$  and lasting for only about 1 Myr.

Figure 2 illustrates the star formation process in the FD simulation. At  $t = 5$  Myr, gravitational instability leads to the formation of numerous small and medium-sized gas clumps, particularly in the nuclear region. Concurrently, a significant number of star particles emerge. As time progresses, these gas clumps grow and spawn more star particles. Clumps merge to form larger clumps, and star particles would form super star clusters. By 15–20 Myr, a substantial number of



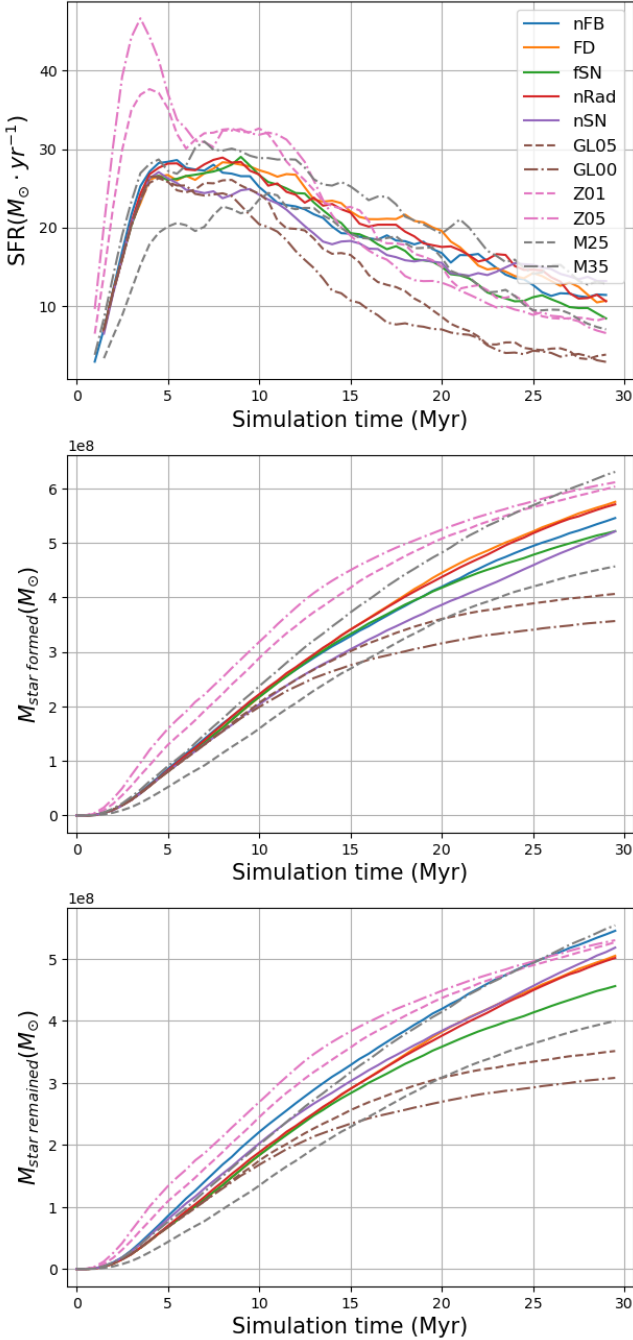


**Figure 3.** Top: The star formation rate as functions of time in various simulations. Middle: The total mass of stars formed as a function of time. Bottom: The total mass of stars formed in the starburst but still exist, i.e. not explode as SNe, as a function of time.

stars and clusters have formed, leaving only a small volume occupied by dense gas.

The top panel of Figure 3 quantitatively illustrates the star formation history (SFH) in our simulations. Most simulations exhibit a rapid increase in the star formation rate (SFR) from nearly zero at  $t = 2$  Myr to a peak of  $20\text{--}30 M_{\odot} \text{ yr}^{-1}$  at  $t \sim 5$  Myr, followed by a gradual decline to around  $4\text{--}12 M_{\odot} \text{ yr}^{-1}$  at  $t \sim 30$  Myr. Compared to Schreiber et al. 2003, our simulated starburst exhibits a flatter profile,

a lower peak SFR, and a longer duration. The top panel of Figure 3 also highlights the impact of different feedback processes, gas return, initial gas disc mass, and initial metallicity on the SFH.

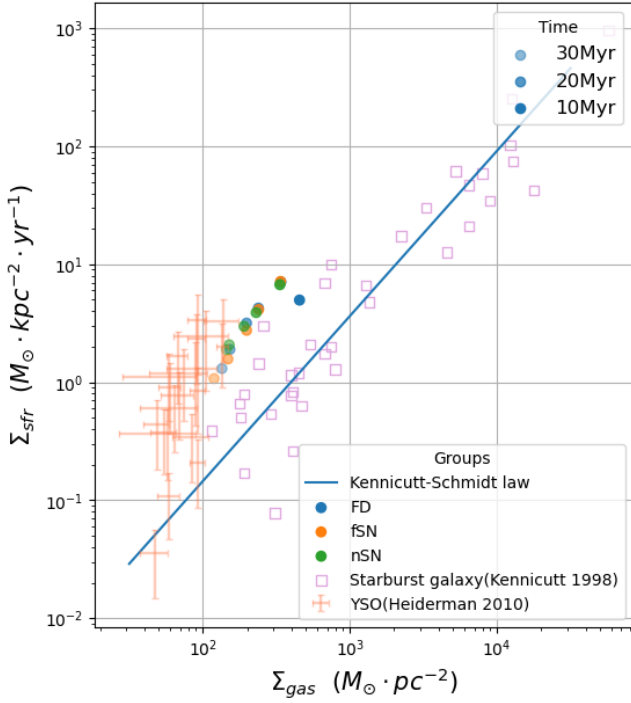
Disabling any single stellar feedback mechanism has a minor effect on the SFH. However, disabling all three feedback processes will reduce the SFR by  $5 \sim 10\%$ , which seems somewhat abnormal. Meanwhile, switching to a fixed SNe energy model, which injects roughly twice the energy of the fiducial variable SNe model, moderately reduces the SFR after  $t \sim 10$  Myr. The probable reason is that stellar feedback with moderate strength can positively influence star formation. However, excessively strong feedback can suppress star formation activity. We conclude that the overall SFH of the starburst is moderately impacted by the stellar feedback implemented in our simulation. This is likely because, on the starburst timescale of 30 Myr, the initial conditions of the gas disc and the gas return process, which determine the amount of gas can collapse, have a stronger influence.

Figure 3 shows that reducing the gas return fraction from 100% to 50% and 0% significantly lowers both the SFR and SFE, as a substantial fraction of gas becomes locked in stars. Meanwhile, varying the initial metallicity  $Z_{\text{init}}$  notably impacts the SFH. Higher initial metallicity leads to faster cooling, resulting in a more violent starburst during the first 15 Myr, with peak SFRs of  $37 M_{\odot} \text{ yr}^{-1}$  in the Z01 simulation and  $45 M_{\odot} \text{ yr}^{-1}$  in Z05. However, this intense early starburst is followed by rapid quenching after  $t > 15$  Myr, leading to a final star formation efficiency (SFE) and total stellar masses similar to those of the fiducial run (FD). In addition, increasing  $M_{\text{gd}}$  will moderately enhance the SFR at  $t > 15$  Myr, while a lower  $M_{\text{gd}}$  will suppress star formation activity throughout the simulation.

The middle panel of Figure 3 presents the total stellar mass formed as a function of time. At  $t \sim 30$  Myr, the total stellar mass in most simulations ranges from  $5.0 \times 10^8 M_{\odot}$  to  $6.0 \times 10^8 M_{\odot}$ , corresponding to a total input of SN energy of  $2.3 \sim 2.7 \times 10^{57} \text{ erg}$  for the variable SN model and  $\sim 4.7 \times 10^{57} \text{ erg}$  for the fixed SN model. Reducing the gas return fraction to 50% or 0%, or adopting a lower gas disk mass of  $M_{\text{gd}} = 2.5 \times 10^9 M_{\odot}$ , results in a lower total stellar mass of  $3.5 \times 10^8 M_{\odot}$  to  $4.5 \times 10^8 M_{\odot}$ . This implies that approximately 12%–20% of the initial gas disk mass was converted into stars over 30 Myr. Observational estimates of the total stellar mass formed during the past  $\sim 15\text{--}30$  Myr range from  $2.0 \times 10^8 M_{\odot}$  to  $3.5 \times 10^8 M_{\odot}$  (Rieke et al. 1993; Schreiber et al. 2003; Strickland & Heckman 2009), which is broadly consistent with our simulations with reduced gas return fractions or lower initial gas disk masses. However, observational estimates of the SFH are subject to uncertainties due to factors such as dust absorption, projection effects, and assumptions about the initial mass function and stellar evolution (e.g. Schreiber et al. 2003).

Another way to compare our results with observational constraints is to examine the total mass of stars formed during the starburst that remain within the nuclear region. The bottom panel of Figure 3 shows the stellar mass within  $r < 1000$  pc as a function of time in our simulations, suggesting that  $\sim 20\%$  of the formed stellar mass has either undergone SN explosions or escaped from the nuclear region. At  $t = 30$  Myr, the total remaining stellar mass within  $r < 1000$  pc ranges from  $3.0 \times 10^8 M_{\odot}$  to  $6.0 \times 10^8 M_{\odot}$ , which is below the total mass in the nuclear region (within  $\sim 500\text{--}600$  pc) estimated by Schreiber et al. (2001).

In addition, we explore the relation between the surface SFR density,  $\Sigma_{\text{SFR}}$ , and cold gas surface density,  $\Sigma_{\text{gas}}$ , in our simulations to assess the validity of our star formation and feedback models. As shown in Figure 4, the  $\Sigma_{\text{SFR}}$  at a fix  $\Sigma_{\text{gas}}$  in our simulations is 6 to 8 times higher than predicted by the classical Kennicutt-Schmidt law, but aligns well with the  $\Sigma_{\text{SFR}}\text{--}\Sigma_{\text{gas}}$  relation observed in some



**Figure 4.** The surface star formation rate density against the surface gas density in the FD (filled blue circle), fSN (filled yellow circle) and nSN (filled green circle) simulations, with respect to the Kennicutt-Schmidt law (solid blue line), star burst galaxies in Kennicutt 1998 and young stellar objects in Heiderman et al. 2010.

of the starburst galaxies with highly efficient star formation activity. This elevated star formation activity may be attributed to several factors, including the excessively high surface density and the overall collapse or contraction of the nuclear region.

### 3.2 properties of the star clusters

The properties of star clusters formed during the starburst can significantly influence the launch and development of galactic outflows. Previous studies have employed super star clusters (SSCs) to drive galactic winds in M82-like galaxies (Melioli et al. 2013; Schneider et al. 2020; Schneider & Mao 2024). To investigate the properties of star clusters formed in our simulations, we utilize the friends-of-friends (FoF) algorithm to identify clusters and analyze their spatial distribution, metallicity, mass function (CMF), and other characteristics.

The top panel of Figure 5 presents the cumulative CMF in our simulations. Recent JWST observations by Levy et al. (2024) suggest a power-law CMF for star clusters in M82,  $y \propto -\alpha \log x$ , with a slope of  $\alpha = 0.9 \pm 0.2$ . Our simulated CMF exhibits a more bottom-heavy distribution. This discrepancy may be attributed to the imposed mass threshold,  $M_{\text{env}}$ , when converting a sink particle to a star particle. The higher-mass end of the CMF, less affected by this threshold, aligns better with the observed power-law slope of  $\alpha = 0.9$ .

While Section 3.1 demonstrates that stellar feedback has a modest impact on the overall SFH, it significantly influences the cumulative CMF. Simulations nRad and nFB exhibit a more top-heavy CMF compared to other simulations, suggesting that stellar feedback effectively disrupts gas accretion in giant star-forming clumps, re-

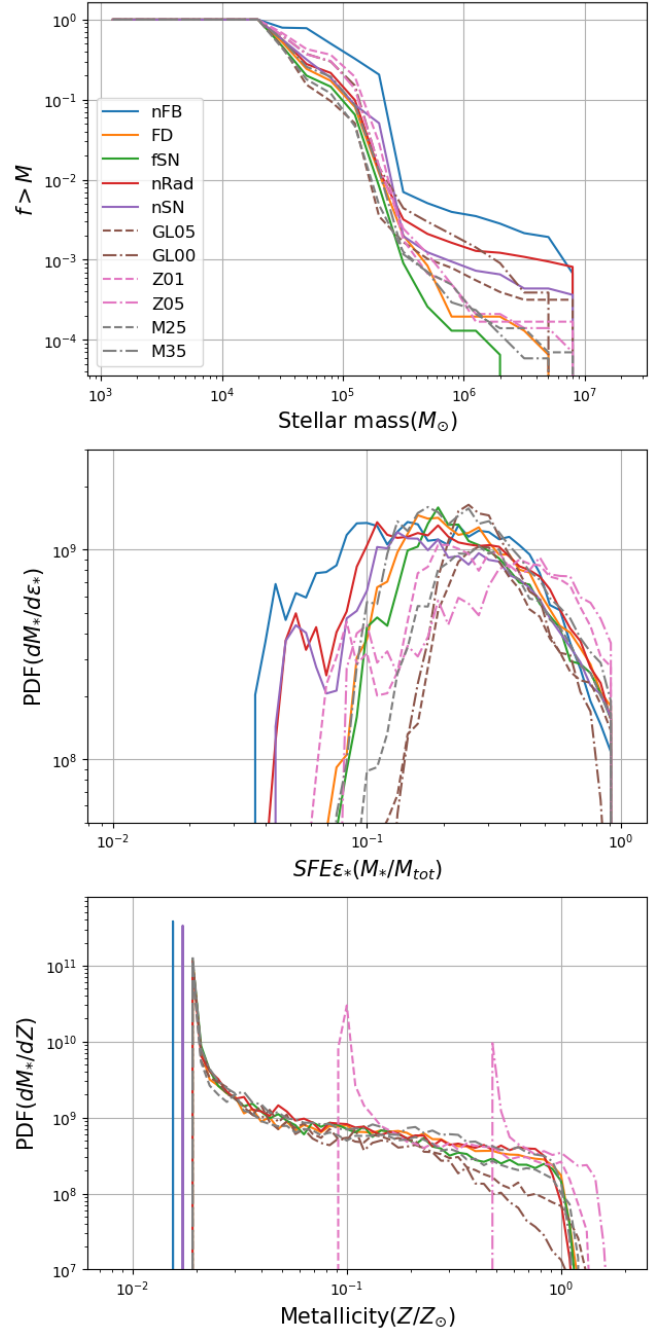


**Figure 5.** Top: the cumulative star cluster mass function in various simulations. Middle: the distribution of integrated star formation efficiency in sink/star particles. Bottom: The distribution of stellar metallicity in various simulations. The metallicity in nFB and nSN are  $0.02Z_{\odot}$ , which has been shifted leftward slightly in the plot for the sake of clarity.

distributes gas, and inhibits the formation of massive star clusters. Among the three feedback mechanisms, radiation feedback appears to be the most effective in suppressing the formation of SSCs, reducing the fraction of SSCs with masses exceeding  $M_* > 10^6 M_{\odot}$  by 90%, and eliminating those with masses above  $M_* > 10^7 M_{\odot}$ . In contrast, the default variable SNe feedback mode has a more moderate impact on the formation of massive SSCs.

On the other hand, all three stellar feedback mechanisms can sup-

press the integrated star formation efficiency (SFE) within individual sink particles. The middle panel in 5 across various simulations, which follows a roughly log-normal pattern. The median integrated SFE ranges from 10% to 30%, which is generally consistent with previous simulations (Dale et al. 2014; Li et al. 2019; Fukushima & Yajima 2021), but higher than observational estimates of (Chevance et al. 2020). This discrepancy may be partly attributed to our assumption of a 20% star formation efficiency per free-fall time for all sink particles, regardless of their properties.

Compared to the FD simulation, disabling either radiation feedback or SNe feedback results in a higher fraction of star clusters with integrated star formation efficiencies below 0.1. This suggests that sink particles in these simulations accrete gas at a faster rate than in the FD run, accumulating 5-10 times more gas mass before being converted to star particles. These findings underscore the importance of radiation feedback and SNe feedback in suppressing gas accretion onto star-forming clumps.

The metallicity of newly formed stars in the nuclear region provides insights into the properties of the starburst and the impact of SN feedback. The bottom panel of Figure 5 shows the distribution of stellar metallicities. In simulations without SN feedback, star clusters often retain their initial metallicity. However, in simulations with SN feedback, a significant fraction of star clusters experience metal enrichment, with some reaching metallicities several to tens of times higher than the initial value. In some cases, stars can even attain solar metallicity. Observations by Origlia et al. (2004) indicate that most cool stars in M82's nuclear region have metallicities between  $\frac{1}{10}$  and one Solar metallicity. Their analysis suggests a solar iron abundance and  $\alpha$ -element enhancement for these stars. In our simulations, the median stellar metallicity with core-collapse SN feedback is slightly lower than observed values for an initial gas metallicity of  $Z_{\text{ini}} = 0.02 Z_{\odot}$ , but becomes comparable for  $Z_{\text{ini}} = 0.10 Z_{\odot}$ .

## 4 OUTFLOW

Understanding the evolution of different gas phases during the launch of galactic outflows and the detailed structure of these outflows is crucial for gaining insights into the underlying physics and their impact on the ISM and CGM. In this section, we will examine how gas in various phases is entrained into the outflow and qualitatively assess the properties of the galactic outflow in our simulations. We will also investigate the effects of different feedback mechanisms, gas return fractions, and initial gas disk masses on the development of the outflow.

### 4.1 Launch of the kpc scale multiphase wind

Figures 6 and 7 provide detailed insights into the launch of the multiphase outflow in the starburst region of the FD simulation. Generally, the launch of galactic winds in our simulations occurs in two stages: the formation and breakout of a superbubble foam, followed by the development of a kpc-scale multiphase wind. Figure 8 presents an edge-on view of the second stage, showcasing the formation of the kpc-scale outflow.

The first stage, spanning from  $t \sim 5$  Myr to  $t \sim 15$  Myr, involves the formation and breakout of a superbubble foam. Initially, the turbulent ISM is dominated by cool gas residing in low-density voids, high-density filaments, and very dense clumps. A few isolated supernova remnants (SNRs) emerge around 5 Myr, expanding into the cool ISM. As shown in the top right panel of Figure 6, these SNRs form within dense clumps, leading to significant metal enrichment

of the surrounding cool gas. The lower-density ISM in the voids is more easily ionized and expelled outward. As more SNe occur, their remnants merge to form a superbubble foam. Between  $t = 10$  and 12.5 Myr, a single superbubble dominates the central starburst region, filled with warm and hot gas and permeated by high-density cool filaments (see the temperature panels in Figures 6 and 7). This superbubble expands and eventually breaks through the dense gas disk before  $t \sim 15$  Myr, with outflowing gas reaching heights of 500 pc.

Following the superbubble breakout, hot gas moves outward along the minor axis of the disk at the highest velocity, followed by warm gas, and then cool gas in tenuous filaments. Figure 7 illustrates the significant interaction and mixing between cool filaments and the hot phase in the outflow, which contributes to the acceleration of the cool phase (Schneider et al. 2020; Fielding & Bryan 2022). As the filaments are stretched, their lengths increase, reaching hundreds of parsecs by  $t = 15$  Myr. These filament features in the wind are remarkably similar to recent JWST observations (Bolatto et al. 2024).

While the visual appearance of these cool filaments in the wind bears some resemblance to previous simulations of M82's wind (e.g., Cooper et al. 2008; Melioli et al. 2013; Schneider et al. 2020), the formation and evolution of these filaments in our simulations differ from previous work, which often attributed their formation to the interaction between spherical cold clouds and the hot wind. For instance, Cooper et al. (2008) shows that small, spherical cold clouds, formed from the disruption of larger gas clouds, are entrained into the outflow. These spherical clouds are then stretched by ram pressure to form filaments.

Our picture align with previous simulations of giant molecular cloud disruption at resolutions of 0.01-0.1 pc (see, e.g., Kim et al. 2018; Li et al. 2019; Fukushima & Yajima 2021). These studies demonstrate that feedback from massive stars ionizes and expels low-density gas within GMCs, while high-density filamentary structures can survive. However, our simulation's 4 pc resolution limits its ability to resolve cloud structures on parsec scales. Therefore, both cool gas in filamentary structures with length of a few to 100 pc, and smaller, nearly spherical clouds may survive the feedback from the starburst. As the warm and hot phases expand outward, both cool filamentous and cloud-like structures can be entrained into the outflow, contributing to the formation of the observed cool filaments in the M82's wind.

The multiphase wind comprises not only hot and cool phases but also a considerable amount of warm gas. Some of this warm gas originates from the disk, while other portions arise from the mixing layer between the hot and cool phases. Additionally, stellar feedback, primarily from core-collapse SNe, effectively enriches the ISM in the central region. By  $t = 15$  Myr, a substantial fraction of the multiphase gas in the sub-kpc wind has been enriched to metallicities exceeding solar. Subsequently, even more gas in the wind attains super-solar metallicities.

After the super bubble foam breaks out, the second stage, the formation of a kpc-scale multiphase wind, takes another 10-15 Myr. From  $t = 15$  Myr onward, the wind continues to expand outward. This multiphase outflow consists of volume-filling hot gas, mass-dominant cold gas, and warm gas. As shown in Figure 8, the multiphase outflow extends beyond 1.5 kpc by  $t = 20$  Myr. By  $t = 25$  Myr, the outflow in the fiducial run FD reaches the upper boundary of the simulation volume (2 kpc along the minor axis), with numerous cool filaments stretching beyond 1 kpc. The outflow base has a radius of approximately 1.5 kpc. While some gas may escape the simulation volume by  $t = 30$  Myr, the limited volume size and simulation time restrict our ability to fully capture the long-term evolution of the outflow.



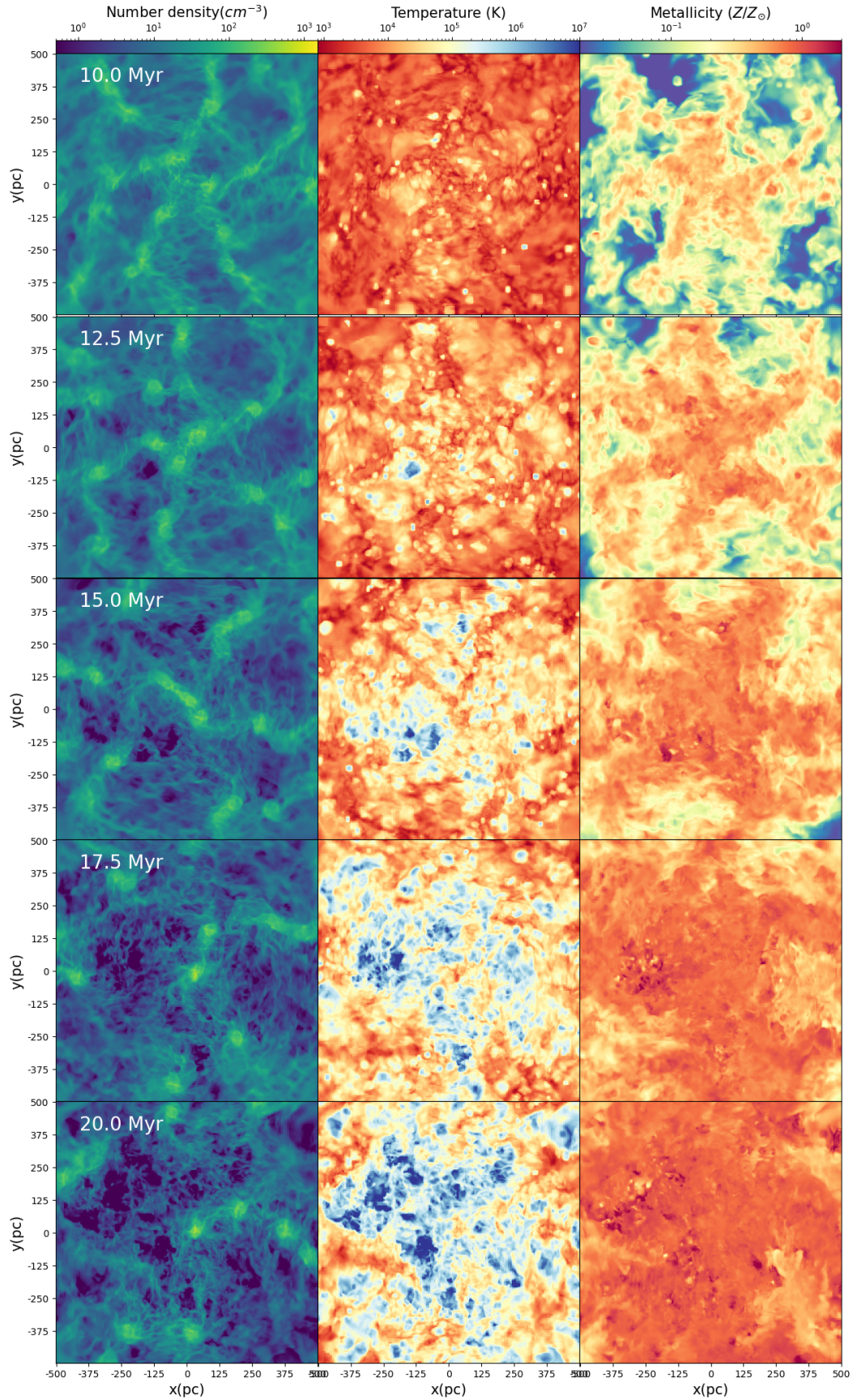


**Figure 6.** Face-on view of the central region of simulation FD. The left, middle, and right columns show the gas density, temperature, and metallicity. From the top to the bottom row, results at time  $t=10, 12.5, 15.0, 17.5,$  and  $20.0$  Myr are shown.



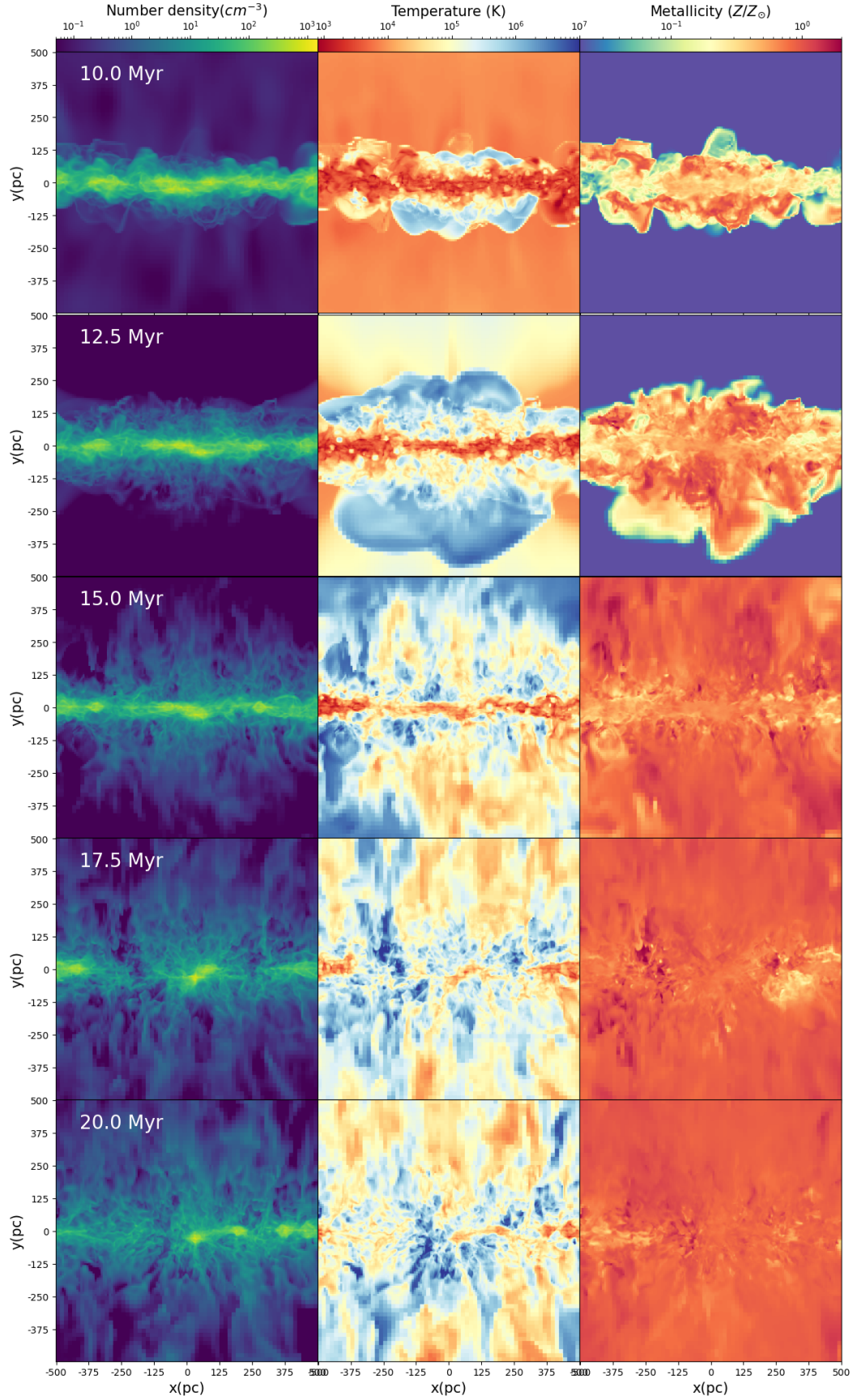


**Figure 7.** Edge-on view of the central region of simulation FD. The left, middle, and right columns show the gas density, temperature, and metallicity. From the top to the bottom row, results at time  $t=10, 12.5, 15.0, 17.5,$  and  $20.0$  Myr are shown.

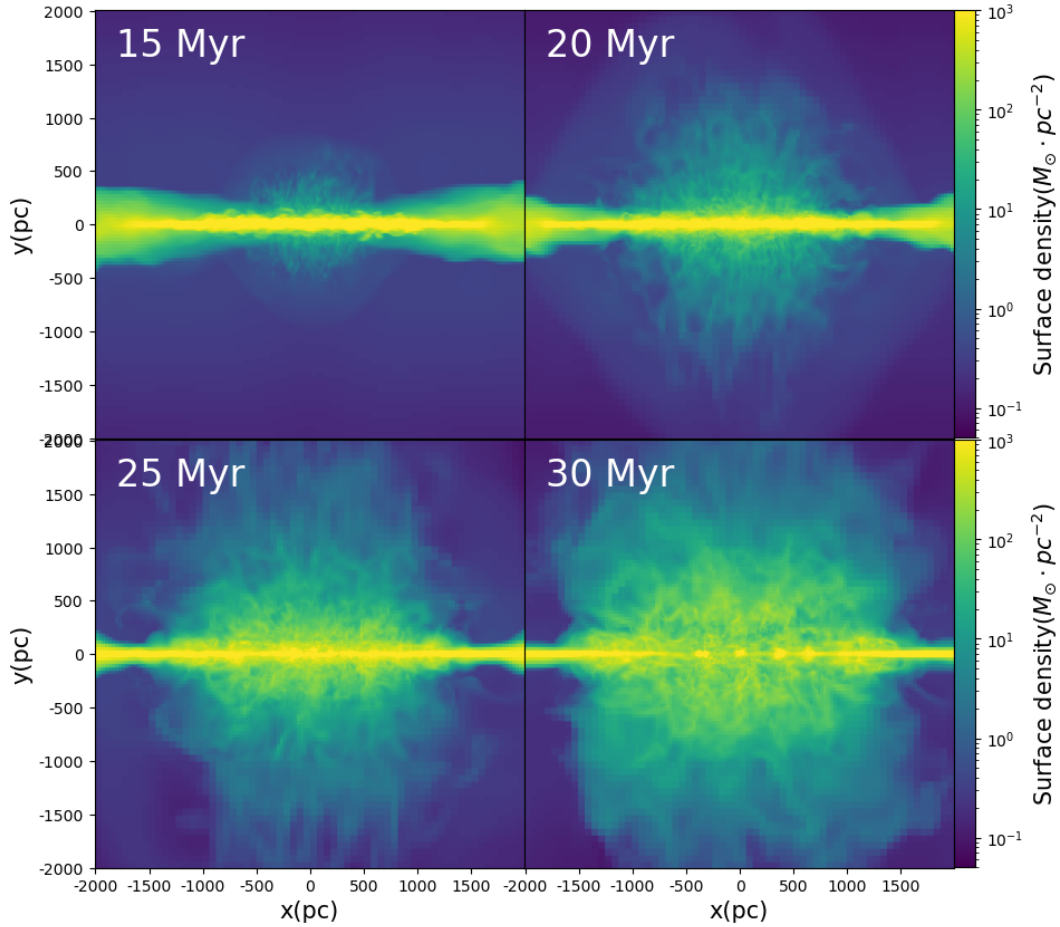


**Figure 8.** Edge-on view of the projected gas density in simulation FD. The four images show how galactic wind is launched in the widespread area across the galactic disk, eventually forming an outflow structure stretching to the edge of the simulated zone.

#### 4.2 Evolution of different phases in the wind

The origin of the cool and cold gas in galactic winds remains a topic of debate. Some studies propose that the cold phase originates from the cooling of the hot ionized phase (e.g. [Thompson et al. 2015](#)), while others suggest that it arises directly from accelerated fragments ejected from the disk (e.g. [Fujita et al. 2008](#); [Martini et al. 2018](#)). These cold phases are then further accelerated through interactions with the hot phase. Our simulations demonstrate that most of the cool and cold gas in the wind originates directly from the disk. In the following subsections, we delve deeper into the evolution of different gas phases in the wind.

Figure 9 shows the distribution of the velocity along the minor axis, denoted as  $V_z$ , for the cool ( $T < 2 \times 10^4$  K, top panel), warm ( $2 \times 10^4$  to  $2 \times 10^5$  K, middle panel), and hot ( $T > 2 \times 10^5$  K, bottom panel) gas phases at different distances from the minor axis,  $r$ , in the FD simulation at 30 Myr. From left to right, the panels show results at heights of 500, 1000, 1500, and 2000 pc. A significant difference in the  $V_z$ - $r$  space from  $z=500$  to  $z=2000$  pc is observed between the cool gas and the other two phases. At  $z = 500$  pc, most of the cool gas has a vertical velocity between  $\sim 80 \text{ km} \cdot \text{s}^{-1}$  and  $\sim 300 \text{ km} \cdot \text{s}^{-1}$ , which increases moderately with height. This velocity is well below the escape velocity, suggesting that most of the cool gas in the wind will eventually fall back onto the disk.

In comparison, [Martini et al. \(2018\)](#) found that the line-of-sight

velocity of most HI in the M82 wind is around  $150 \text{ km} \cdot \text{s}^{-1}$  at  $z = 0.5$  kpc and  $50 \text{ km} \cdot \text{s}^{-1}$  at  $z = 1$  kpc. Considering that M82 has an inclination angle of  $77 \pm 3^\circ$ , these correspond to vertical velocities  $V_z$  around  $550 \text{ km} \cdot \text{s}^{-1}$  and  $200 \sim 300 \text{ km} \cdot \text{s}^{-1}$ , respectively. Observations of H- $\alpha$  emission indicate that the three-dimensional radial outflow velocity of gas with a temperature of  $10^4$  K is roughly  $150 \text{ km/s}$  at  $r \sim 0.5$  kpc, rising to  $500\text{--}600 \text{ km/s}$  at  $r \sim 1.0$  kpc, and remaining relatively constant in the outer regions ([Xu et al. 2023b](#)). Our simulated velocities for the cool phase are approximately 30%–50% of the observed values.

In contrast, the warm and hot gas in our simulations exhibits higher vertical velocities. Most warm gases have velocities between  $300 \sim 600 \text{ km} \cdot \text{s}^{-1}$ , while hot gas velocities range from  $600 \sim 1000 \text{ km} \cdot \text{s}^{-1}$ . A significant fraction of the warm and hot ionized gas in the wind can escape the galaxy’s potential well. However, the velocities of the hot gas in our simulations are still about 20%–30% lower than those inferred from X-ray observations of M82 ([Strickland & Heckman 2009](#)).

To investigate the origin of the cool gas in the outflow, we compare the net inflow rate with the time variation of the gas mass within three height zones along the minor axis: 500–1000 pc, 1000–1500 pc and 1500–2000 pc. Figure 10 shows that the net inflow rates closely match the growth rates of cool gas in these zones, indicating that most of the cool gas in the wind originates from the disk rather than cooling from the warm and hot phases. While some warm and hot gas can

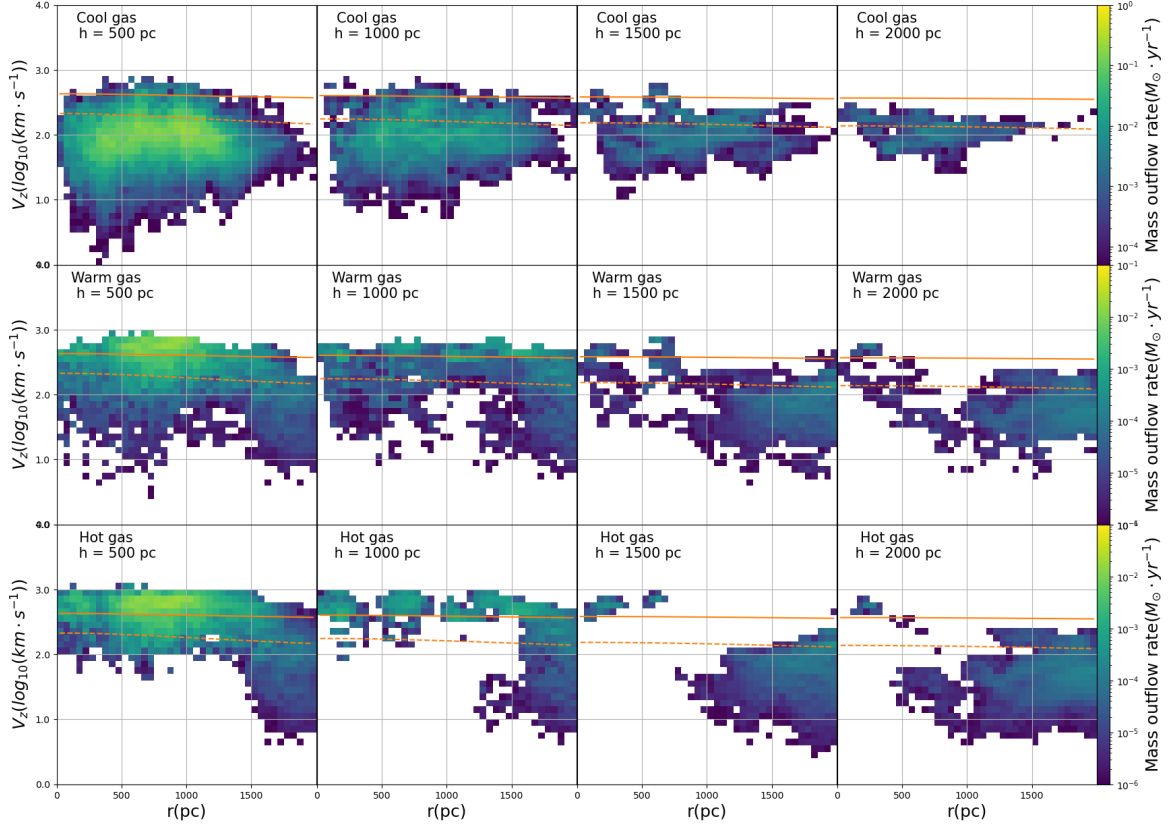


**Figure 9.** The outward velocity distribution of cool ( $T < 2 \times 10^4$  K, top), warm ( $2 \times 10^4$  K  $< T < 2 \times 10^5$  K middle) and hot ( $T > 2 \times 10^5$  K, bottom) gas at  $t = 30$  Myr at different distance,  $r$ , from the minor axis. From the left to the right columns, results at a height of 500, 1000, 1500, and 2000 pc are shown. The color indicates the mass outflow rate in each  $r$ - $v_z$  bin.

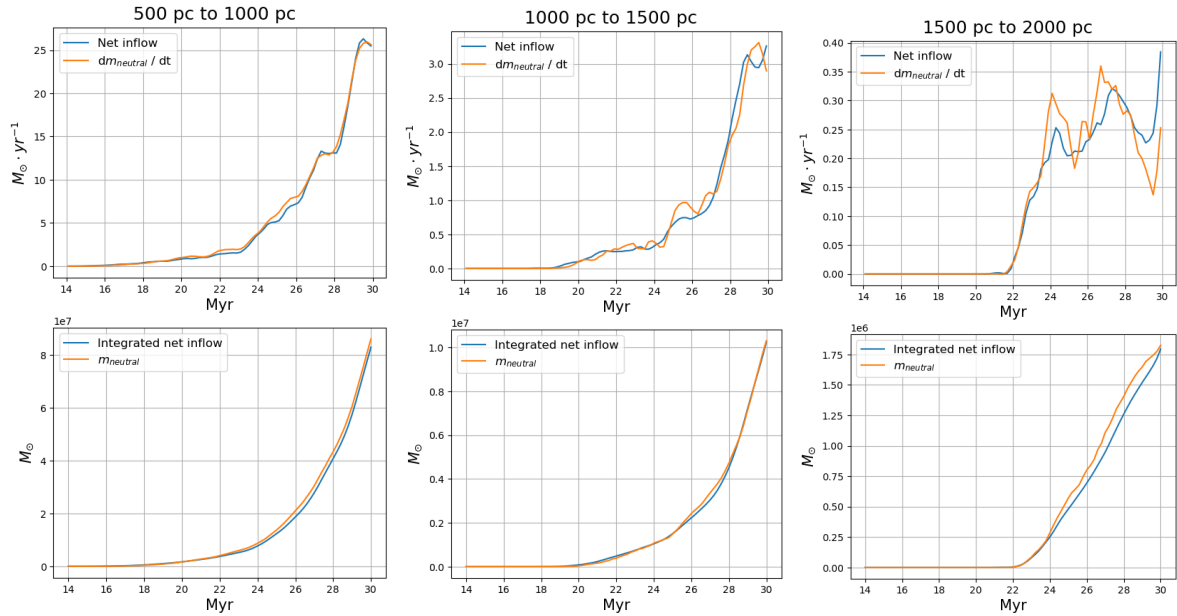


**Figure 10.** Top: Blue lines indicate the net inflow rate of cool ( $T < 2 \times 10^4$  K) gas into three zones of a height between 500 to 1000 pc (left), 1000 to 1500 pc (middle) and 1500 to 2000 pc as functions of time, while the yellow line indicate the time variations of cool gas mass in corresponding zone. Bottom: Same as the top row, but for the integrated net inflow rate and the total cool gas mass.

cool and contribute to the cool phase, as shown in the lower right panel of Figure 10, their overall contribution to the cool phase in the outflow is relatively minor.

We also analyzed the metallicity distribution of the three phases in the outflow (figure not shown). The three phases exhibit similar metallicity distributions, with most gas having a metallicity of  $Z \sim 0.5 - 2.0 Z_{\odot}$ , approximately 50-100 times higher than the initial metallicity in the FD simulation. This indicates that all gas in the outflow has undergone significant metal enrichment.

### 4.3 Overall feature of the outflow in various simulations

The launch of galactic winds varies significantly across different simulations. To investigate the impact of different feedback mechanisms, Figures 11 and 12 compare the face-on and edge-on views of the wind and disk at  $t = 25$  Myr for simulations with different feedback configurations.

Compared to the FD simulation, the wind in the fSN simulation exhibits a slightly larger opening angle and higher gas density due to the increased total SN energy input. However, the intense SN feedback in the fSN simulation results in a more dispersed gas distribution in the nuclear region. In contrast, the nSN simulation fails to launch a galaxy-scale outflow. Figure 11 shows that the gas disk in the nSN simulation is less turbulent and more concentrated in multiple mini-arms compared to simulations with SN feedback. Although some smaller bubbles filled with warm gas, driven by stellar winds and radiation feedback, are present, only a small amount of gas can escape into the halo, reaching heights of a few hundred to 1 kpc (Figure 12).

When both stellar wind and radiation feedback are excluded (nFB simulation), the gas disk becomes even more compact. In this case, almost no gas from the disk can escape into the halo. Additionally, without SNe, the gas retains its initial metallicity. Figure 13 presents edge-on views of the outflow at 30 Myr for all simulations. Reducing the gas return fraction leads to a decrease in the mass of the outflow. A higher initial gas metallicity results in a larger outflow volume due to enhanced star formation and SN feedback. A less massive gas disk has a modest impact on the strength of the outflow.

### 4.4 Mass and energy outflow rate

The mass and energy outflow rates are crucial properties of galactic winds, as they quantify a galaxy's ability to redistribute baryons and exhibit distinct features in various feedback models. Although many previous simulations have successfully launched galactic outflows in M82-like galaxies, they often struggle to reproduce the observed mass and energy outflow rates of M82. Even recent studies by Schneider et al. (2020) and Schneider & Mao (2024) moderately underestimate the mass outflow rates of the cool and hot phases compared to observational estimates of the wind in M82 (e.g., Leroy et al. 2015; Martini et al. 2018).

We first explore the mass outflow rate of the cool gas. Leroy et al. (2015) derived the mass density function of both HI and H<sub>2</sub>, which is defined as the mass per unit length, by integrating the mass within  $\pm 1.5$  kpc region along the minor axis. To facilitate comparison with their results, we calculate the mass density function of the cool gas at  $t=30$  Myr in our simulations within a 3.0 kpc-wide slit along the minor axis, as shown in the left panel of Figure 14. Furthermore, we measure the mass outflow rate within a narrower 1 kpc-wide slit and compare it to the results of Martini et al. (2018) in the right panel of Figure 14.

The HI+H<sub>2</sub> mass distribution and mass outflow rate at  $z \gtrsim 1000$  pc in simulations using the variable SNe model are approximately 1.5 dex lower than observational estimates. In contrast, simulations with higher energy injection rates, whether from increased initial metallicity or the fixed SNe energy model, can drive cool gas more efficiently, better matching the observed outflow rates below  $z = 1500$  pc. Notably, a higher initial metallicity of  $0.5 Z_{\odot}$  yields a cool gas outflow rate comparable to observations throughout the simulation volume.

However, Section 3 indicates that simulations with a fixed SNe energy model or higher initial gas metallicity produce more stars than observed in M82's recent starburst. To simultaneously replicate both the starburst and outflow characteristics, we need to improve the efficiency of coupling SN energy to the ISM. One potential solution is to incorporate the enhanced feedback effects of clustered supernovae (e.g. Gentry et al. 2017; Fielding et al. 2018). In our subsequent work (Li et al. 2024), we explored the impact of clustered SNe on outflow properties. The inclusion of enhanced feedback from clustered SNe successfully reproduced both the total stellar mass of the starburst and the outflow rates observed in M82.

In addition to the amount of SNe energy injected, the gas supply in the nucleus region of the disk also plays an important role in shaping the properties of outflow. Disabling gas return from star particles drastically reduces the mass of cool gas below 1 kpc and decreases the cool gas outflow rate by a factor of 10 throughout the simulation volume. Meanwhile, a 50% gas return fraction yields a cool gas outflow rate comparable to observations above 1.5 kpc, but significantly lower (by a factor of 10) at 0.5 kpc. The explanations for such features are as follows: a substantial amount of gas is accreted by sink/star particles, depleting the gas supply in the starburst core. Initially, this reduces the resistance to the outflow, but eventually limits the available cool gas to fuel the wind, and hence may increase the outflow rate in the early stage, while lowering the outflow rate in the late stage. In addition, the evolution of outflow rates is not synchronous in different simulations, which can be shown by the results below.

We calculated the total mass and energy outflow rates for all three gas phases as functions of time in each simulation, along with the mass and energy loading factors, which are crucial properties of galactic outflows. The mass and energy loading factors, defined as:

$$\eta_M = \frac{\dot{M}_{out}}{SFR} \quad (21)$$

and

$$\eta_E = \frac{\dot{E}_{out}}{\dot{E}_{SNe}} \quad (22)$$

where  $\dot{M}_{out}$  and  $\dot{E}_{out}$  are the total mass outflow rate and energy outflow rate respectively. Here, both  $\dot{M}_{out}$  and  $\dot{E}_{out}$  are evaluated for all thermal phases across the entire radial extent along the major axis, not just the confined region shown in 14. The results are presented in Figure 15. In simulations with SN feedback, the mass loading factors at  $z = 0.5$  kpc and  $z = 1.0$  kpc are approximately 2-5 and 0.8-5, respectively, at the end of the simulation. The current star formation rate in M82 is uncertain, ranging from  $2-10 M_{\odot} \text{yr}^{-1}$  (e.g. Kennicutt 1998; Leroy et al. 2015). The total mass outflow rate in M82 is estimated to be  $M_{\odot} \text{yr}^{-1}$  at heights of  $z \sim 1-2$  kpc, including the cold, cool, warm, and hot phases (Martini et al. 2018; Strickland & Heckman 2009). This implies a mass loading factor of 1-10 at  $z = 1$  kpc, which is broadly consistent with our simulation results.

The mass loading factor for starburst galaxies with given properties, such as stellar mass, exhibits significant variations across different simulations. This discrepancy can be attributed, in part, to



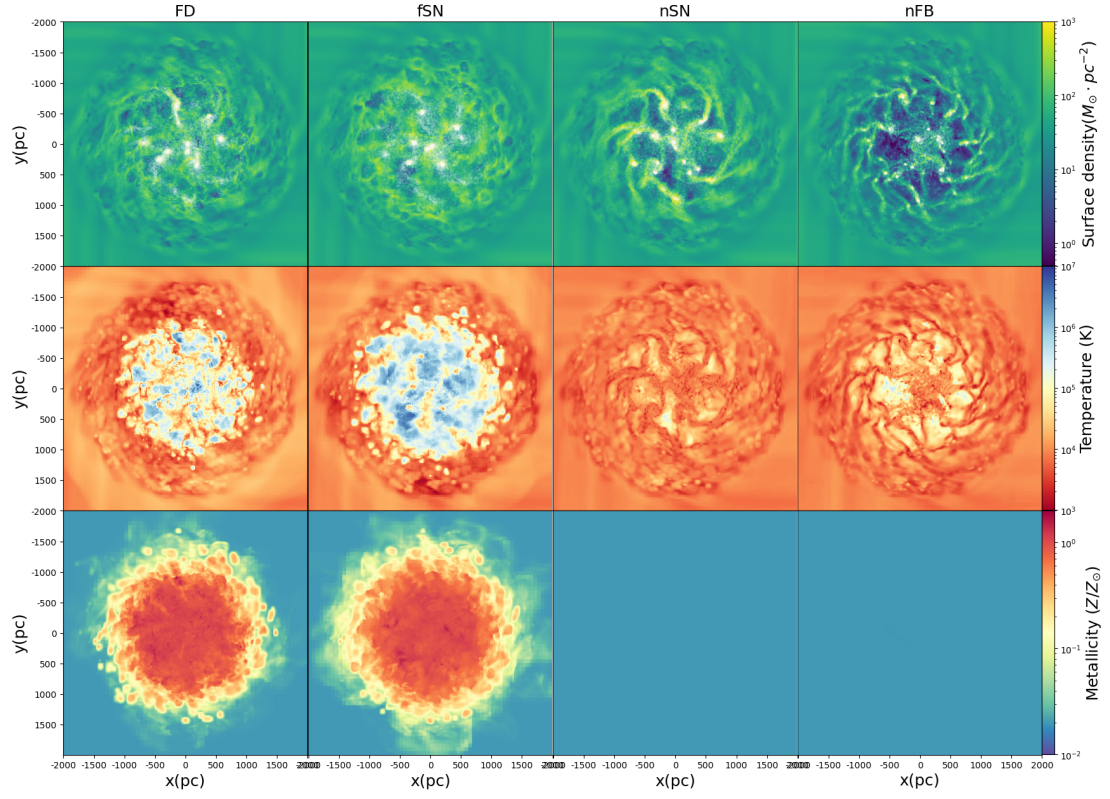


**Figure 11.** Face-on view of different simulations. From the top to the bottom row, column density images of the four major simulations taken at  $t = 25\text{Myr}$ , the corresponding density-weighted average temperature, and density-weighted average metallicity.

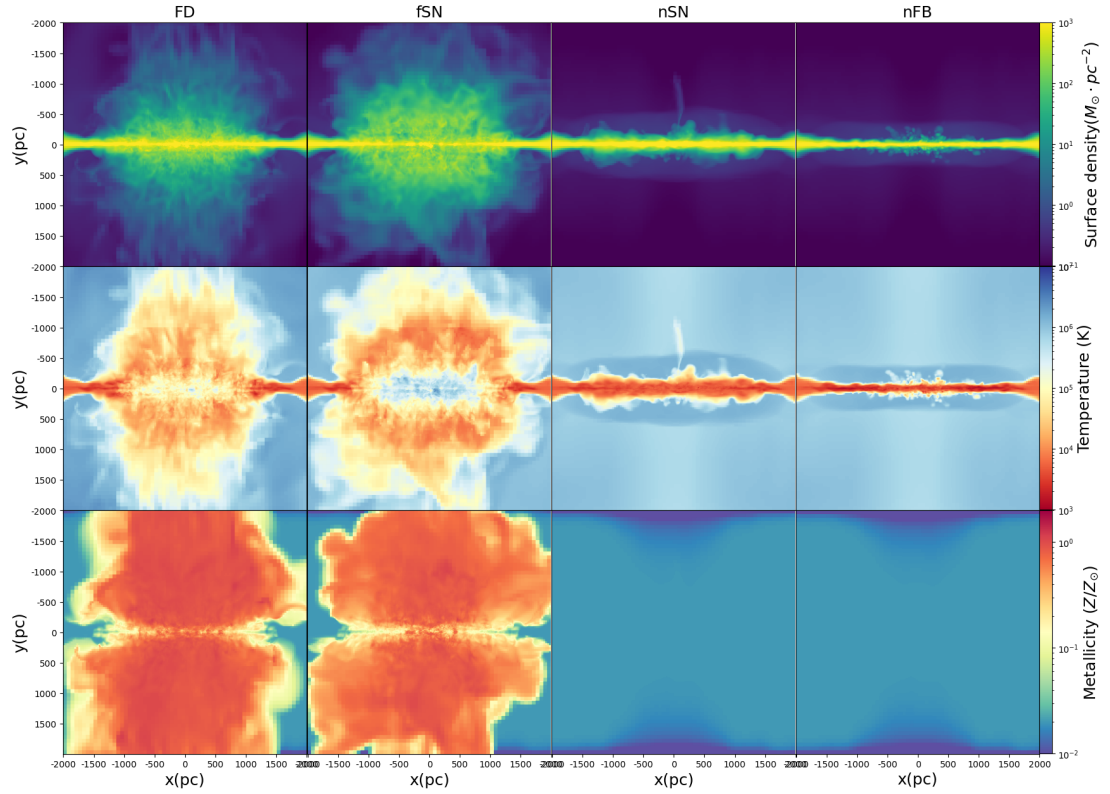


**Figure 12.** Edge-on view of different simulation, similar to Fig 11

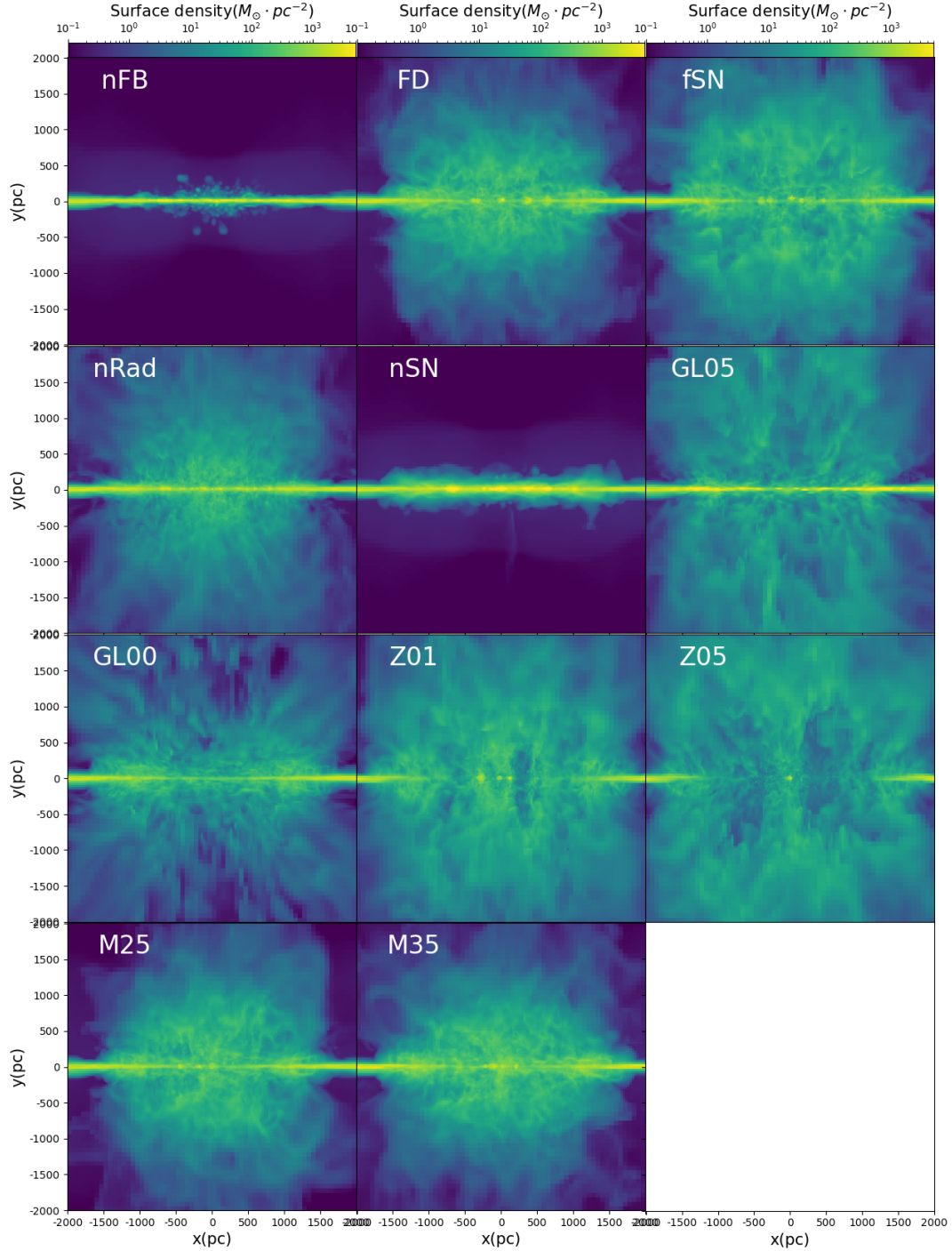


**Figure 13.** Edge-on view of the projected gas density at 30 Myr of all the simulations presented in the main text.

inconsistencies in the methods used to calculate outflow rates. For instance, FIRE-2 simulations employ a spherical shell approach with radii of  $0.10 r_{\text{vir}}$  and  $1.0 r_{\text{vir}}$  (Pandya et al. 2021), while the study based on the EAGLE simulation utilize a more complex Lagrangian particle tracking method (Mitchell et al. 2020). In contrast, the LYRA project adopts a conical approach with a height equal to the simulation box size and a width defined by the star-forming region (Gutcke et al. 2021). These different methodologies can lead to substantial variations in the calculated mass loading factors. We also notice that many simulations have a much longer simulation time than in our

work, allowing galaxies to evolve to a stable state. Therefore, a longer time interval is used in the calculation of the mass and energy loading factor, which can reduce the fluctuations in these measured values.

On the other hand, uncertainties exist in observational estimates of the SFR and mass outflow rate. For example Yuan et al. (2023) suggest that the outflow rates of cold and cool gas in M82 could be uncertain by several times. Furthermore, uncertainties in M82’s inclination angle can introduce systematic errors. To improve the predictive power of simulations, further observational and theoretical

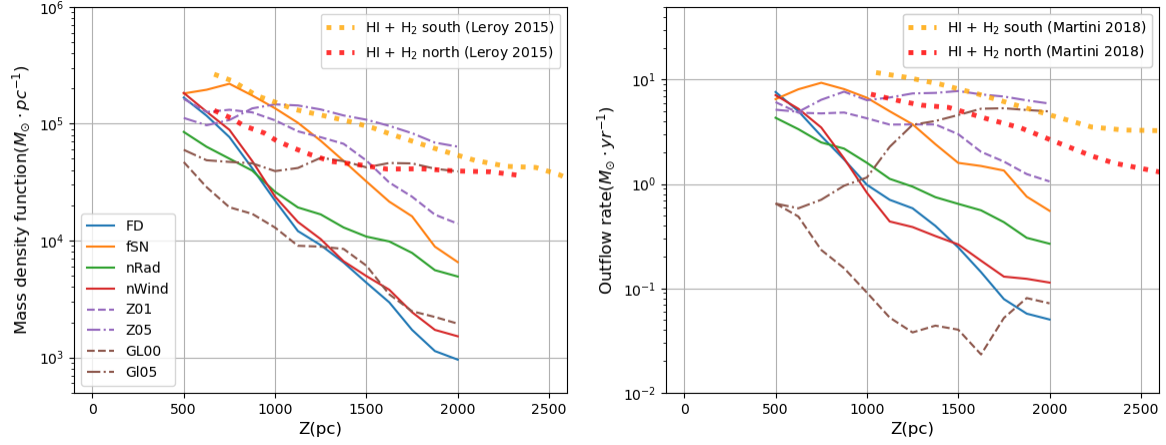


**Figure 14.** Left: the mass density function at  $t = 30$  Myr calculated along the minor axis in various simulations. Right: outflow rate at different heights along the minor axis.

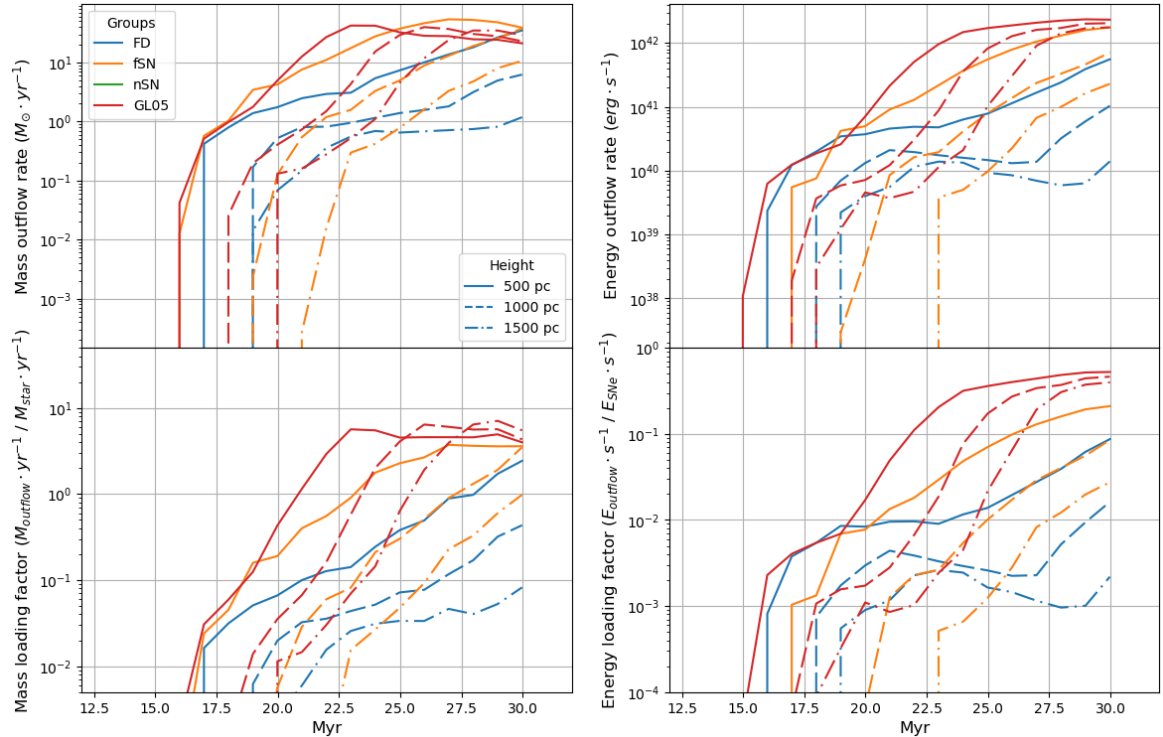


**Figure 15.** The left column: mass outflow rate (upper) and mass loading factor (bottom) in various simulations at the height of 500, 1000, and 1500 pc as a function of time. Right: energy outflow rate (upper) and energy loading factor (bottom). Note that due to the fast self-quenching, the mass loading factor calculated at later times may be over-estimated.

investigations are necessary to reduce these uncertainties and refine our understanding of individual galaxies.

## 5 DISCUSSIONS

### 5.1 Comparison with previous simulation

The multiphase outflow driven by starburst in M82 has been studied in a number of simulation works in the past two decades (e.g. Cooper et al. 2008; Melioli et al. 2013; Schneider et al. 2020; Schneider & Mao 2024). In comparison to previous studies, the most important

improvement in our work is that the star formation process and related feedback are solved self-consistently. More specifically, stars are formed in dense collapsing gas clumps that emerge from the evolution of the gas disc due to gravitational instability. The formation of stars and consequent feedback are handled by the sink particle module. As a result, the stars formed in our simulation are highly coupled with the dense clouds, allowing us to resolve the early phases in the launch of the outflow in great detail. This includes examining how wind bubbles and SN bubbles expand and break through dense clouds where stars are embedded, as well as how isolated bubbles merge and drive the outflow during the early stages.

Moreover, the launch of cool filaments in our simulations shows some notable features that have not been revealed by previous simulations of the galactic winds. In previous studies (e.g. [Cooper et al. 2008](#)), the cold filaments in the outflow were thought to result from the interaction between the hot phase and strings of nearly spherical small dense clouds, which are fragments of the giant clouds in the central disk and were drawn out to the outflow. Due to ram pressure, gas in the cold clouds is stripped and entrained into the hot wind, forming filaments. However, in our simulations, the cold and cool filaments in the wind rarely consist of a dense core. Instead, most of them originated as filaments in the turbulent ISM residing in the nuclear region before being pulled into the outflow. These filaments survived the growth and merge of hot bubbles produced by SNe feedback in the starburst region. The reason why there is barely any small-size cloud remaining in the starburst region in our simulations is as follows: first, the star particles are formed around the density peak of dense gas clumps, and hence the stellar feedback would be more effective in destroying the cores of gas clumps; second, the limited resolution in this work cannot resolve clouds with a size of several parsecs.

Our picture of the survival of cool filaments in the starburst region is consistent with previous high-resolution simulations of the destruction of individual GMCs, with a resolution of about 0.01-0.1 pc. Those simulations show that a considerable fraction of the high-density filamentary structures in the GMCs can survive the feedback from newly born massive stars (see, e.g., [Kim et al. 2018](#); [Li et al. 2019](#); [Fukushima & Yajima 2021](#)). We argue that it is probable that both the filamentary structures with length of a few to 100 pc and nearly spherical small cloud/clumps with size a few parsecs, harboring cool and cold gas and residing in the nuclear region before the starburst, can survive the feedback from newly born massive stars, and can then be entrained into the multiphase outflow, and both contribute to the cool filaments in the galactic winds.

## 5.2 Limitation of this study

We note that there are several limitations in our current work. First, the recipes and parameters adopted in several processes, such as the star formation, various feedback mechanisms, and gas return, have not been well justified by theory or observations and hence are somewhat arbitrary. The properties of the star clusters and the effect of clustered SN would be different if these recipes and parameters were changed. Second, our model of M82 has not incorporated the tidal interactions between the three members in the M81 group, which would lead to the initial conditions in our simulations deviating from the real case to some extent, especially in the central region. However, we expect that this factor may only change the time scale and peak of the starburst moderately and do not have a significant impact on the launch of outflow. Third, the side length of our simulation box is 2 kpc, which is unable to track the development of wind at a larger radius, and the current results also may have suffered from some boundary effect. Lastly, our current simulation only treats the stars formed in previous starbursts as a gravity potential background, while neglecting the feedback from those stars. With a total mass around  $3 - 5 \times 10^9 M_\odot$ , the older stars could potentially prevent clustering and suppress star formation to a certain degree through type Ia supernovae and IR radiation.

Furthermore, there are several shortcomings in the results of our simulations, with respect to the observations of the recent nuclear starburst and outflow in M82. The total stellar mass formed in the starburst in many of our simulations is higher than the value estimated from observations. However, this issue can be resolved if the average

gas return fraction of star-forming clumps is reduced to 0% – 50% or with a reduced initial gas mass of  $2.5 \times 10^9 M_\odot$ . Moreover, the outflow velocity in our simulations is slower than in the observations. This situation is worse for the cool gas, which is only one-third to half of the observed value. In addition, the outflow rate of the cool gas in many simulations is lower than that observed at the height  $z \gtrsim 1$  kpc. Although our simulations can form super star clusters, the limited resolution is likely unable to capture the enhanced feedback efficiency due to clustered SNe as demonstrated in previous studies ([Gentry et al. 2017](#); [Fielding et al. 2018](#)), probably due to overcooling.

In the second paper of this series, we carry out simulations in a large volume and with a different recipe to couple the SN feedback energy to the neighbouring ISM, and to return the gas in sink/particles to the ISM. We find that a better agreement with the observations on the total stellar mass and outflow rate can be obtained by moderate revisions on the related modules and the inclusion of the enhanced feedback effect because of clustered SNe. More details can be found in [Li et al. 2024](#). However, we find that further improvement is needed to increase the outflow velocity of cool and cold gas in the wind.

## 6 CONCLUSIONS

In this work, we conducted high-resolution hydrodynamical simulations to investigate the recent starburst and the subsequent launch of a galactic-scale wind in M82. Unlike previous studies that relied on prescribed starburst models, we self-consistently resolved the star formation process using a sink particle module. We explored the impact of various factors, including different feedback mechanisms, gas return from sink/star particles into the ISM (destruction of star-forming gas clouds), initial gas metallicity, and gas disk mass, on the starburst and outflow. Our findings are summarized below.

(i) Our simulations successfully reproduce a starburst in the nuclear region, lasting 20-25 Myr with a peak SFR of  $20 - 45 M_\odot \text{ yr}^{-1}$ . The total stellar mass formed in the starburst mostly ranges from  $5 \times 10^8 M_\odot$  to  $6 \times 10^8 M_\odot$ , which is however moderately higher than the value in M82 inferred from observation. However, reducing the gas return fraction to less than 50% or adopting a lower initial gas disk mass of  $2.5 \times 10^9 M_\odot$ , can bring the total stellar mass broadly in line with observations. The observed relation between surface star formation rate and gas surface density in our simulations is several times higher than the classical Kennicutt-Schmidt law but is comparable to that of highly active starburst galaxies and young stellar objects.

(ii) The super star clusters formed in our simulations exhibit a cumulative cluster mass function that agrees reasonably well with observations at the high-mass end. However, the model underpredicts the number of lower-mass clusters. The median integrated star formation efficiency of star particles ranges from 10% to 30%, which agrees with previous simulations but exceeds observational estimates of 2% to 10%. The metallicity of stars formed in the burst varies from 0.02 to several times solar metallicity, with a mean value of 0.1-0.2 solar for an initial gas metallicity of 0.02 solar. Increasing the initial metallicity to 0.1 solar yields a mean stellar metallicity closer to observed values in M82's nuclear region.

(iii) The launch of the multiphase galactic-scale wind occurs in two stages. The first stage, lasting about 10 Myr, involves the formation and breakout of a superbubble foam composed of hot, warm, and dense, cool filamentary gas. Initially, combined radiation, stellar wind, and SN feedback create numerous small bubbles. The feedback ionizes and heats low-density ISM while leaving the high-density filaments relatively unaffected. Subsequently, these small bubbles merge



to form a large superbubble filled with multiphase gas, including cool filaments. This superbubble eventually breaks out of the disk. The second stage, spanning 10–15 Myr, involves the development of the kpc-scale multiphase outflow. Hot gas expands outward at the highest velocity, followed by warm gas, and then cool gas in filaments. Interactions between the hot phase and cool filaments stretch the filaments. Most of the cool gas in the wind originates directly from the starburst region rather than cooling from the warm and hot phases

(iv) The outflow velocity of cool gas in our simulations is approximately 30 – 50% of the observed values in M82. Similarly, the velocities of warm and hot gas are about 20 – 30% lower than observed. When the galactic wind is fully developed, the mass outflow rate of cool gas in simulations with a total injected SN energy of  $\sim 4 - 6 \times 10^{57}$  erg is comparable to the observations within the range  $500 < z < 2000$  pc. However, simulations with lower SN energy input result in significantly lower cool gas outflow rates. The mass loading factor in most simulations ranges from 0.8 to 5, consistent with observational estimates for M82. To better match both the outflow velocities and rates observed in M82, enhanced feedback efficiency due to clustered SNe is necessary, while simultaneously reducing the total stellar mass formed in the simulation.

(v) SN feedback acts as the primary driver of the outflow, while gas return significantly influences the starburst and outflow properties. The initial mass of gas disc has a moderate effect, while stellar wind and radiation feedback have minor effect on the starburst and the properties of outflow. Radiation feedback can suppress the formation of super star clusters that massive than  $10^7 M_{\odot}$ .

## ACKNOWLEDGEMENTS

We thank the helpful discussions with Antonios, Katsianis and Cheng, Li. This work is supported by the National SKA Program of China (Grant Nos. 2022SKA0110200 and 2022SKA0110202), by the National Natural Science Foundation of China (NSFC) through grants 11733010 and 12173102, and by the China Manned Space Program through its Space Application System. The authors would like to thank National Supercomputer Center in Guangzhou for providing high performance computational resources. Post simulation analysis was performed on the HPC facility of the School of Physics and Astronomy, Sun Yat-Sen University.

## DATA AVAILABILITY

The data underlying this article will be shared on reasonable request to the corresponding author.

## REFERENCES

Agertz O., Kravtsov A., Leitner S., Gnedin N., 2012, *The Astrophysical Journal*, 770  
 Appleton P., Davies R., Stephenson R., 1981, *Monthly Notices of the Royal Astronomical Society*, 195, 327  
 Arribas S., Colina L., Bellocchi E., Maiolino R., Villar-Martín M., 2014, *A&A*, 568, A14  
 Bate M. R., Bonnell I. A., Price N. M., 1995, *MNRAS*, 277, 362  
 Blok W., et al., 2018, *The Astrophysical Journal*, 865, 26  
 Bolatto A. D., et al., 2024, *ApJ*, 967, 63  
 Boldyrev S., 2002, *ApJ*, 569, 841  
 Bondi H., 1952, *Monthly Notices of the Royal Astronomical Society*, 112, 195  
 Cantalupo S., 2009, *Monthly Notices of the Royal Astronomical Society*, 403

Cantat-Gaudin T., Mapelli M., Balaguer-Nunez L., Jordi C., Sacco G., Valenari A., 2018, A ring in a shell: the large-scale 6D structure of the Vela OB2 complex, [doi:10.48550/arXiv.1808.00573](https://doi.org/10.48550/arXiv.1808.00573)  
 Carniani S., et al., 2024, *A&A*, 685, A99  
 Ceverino D., Klypin A., Klimek E., Trujillo-Gomez S., Churchill C., Primack J., 2013, *Monthly Notices of the Royal Astronomical Society*, 442  
 Chevalier R. A., Clegg A. W., 1985, *Nature*, 317, 44  
 Chevanne M., et al., 2020, *MNRAS*, 493, 2872  
 Chynoweth K. M., Langston G. I., Yun M. S., Lockman F. J., Rubin K. H. R., Scoles S. A., 2008, *AJ*, 135, 1983  
 Cole S., Aragon-Salamanca A., Frenk C. S., Navarro J. F., Zepf S. E., 1994, *MNRAS*, 271, 781  
 Cooper J. L., Bicknell G. V., Sutherland R. S., Bland-Hawthorn J., 2008, *ApJ*, 674, 157  
 Cooper J. L., Bicknell G. V., Sutherland R. S., Bland-Hawthorn J., 2009, *ApJ*, 703, 330  
 Crutcher R., Rogstad D., Chu K., 1978, *The Astrophysical Journal*, 225, 784  
 Cuevas Otaola B., Mayya Y., Puerari I., Rosa-González D., 2020, *Monthly Notices of the Royal Astronomical Society*, 500  
 Dale J., Ngoumou J., Ercolano B., Bonnell I., 2014, *Monthly Notices of the Royal Astronomical Society*, 442  
 Das S., Ray A., 2017, *The Astrophysical Journal*, 851  
 Davé R., Anglés-Alcázar D., Narayanan D., Li Q., Rafieferantsoa M. H., Appleby S., 2019, *MNRAS*, 486, 2827  
 Deharveng L., Zavagno A., Schuller F., Caplan J., Pomarès M., Breuck C., 2009, *A&A*, 496  
 Dekel A., Silk J., 1986, *ApJ*, 303, 39  
 Divakara Mayya Y., Carrasco L., 2009, *arXiv e-prints*, p. [arXiv:0906.0757](https://arxiv.org/abs/0906.0757)  
 Dubois Y., et al., 2014, *MNRAS*, 444, 1453  
 Elmegreen B. G., Scalo J., 2004, *ARA&A*, 42, 211  
 Emerick A., Bryan G., Low M.-M., 2018, *The Astrophysical Journal*, 865, L22  
 Emerick A., Bryan G., Mac Low M.-M., 2019, *Monthly Notices of the Royal Astronomical Society*, 482, 1304  
 Federrath C., 2013, *MNRAS*, 436, 1245  
 Federrath C., Roman-Duval J., Klessen R. S., Schmidt W., Mac Low M. M., 2010a, *A&A*, 512, A81  
 Federrath C., Banerjee R., Clark P., Klessen R., 2010b, *Astrophysical Journal - ASTROPHYS J*, 713  
 Fielding D. B., Bryan G. L., 2022, *ApJ*, 924, 82  
 Fielding D., Quataert E., Martizzi D., 2018, *MNRAS*, 481, 3325  
 Fluetsch A., et al., 2019, *MNRAS*, 483, 4586  
 Fujii M., Saitoh T., Hirai Y., Wang L., 2021, *Publications of the Astronomical Society of Japan*, 73  
 Fujita A., Low M.-M., New K., Weaver R., 2008, *The Astrophysical Journal*, 698  
 Fukushima H., Yajima H., 2021, *MNRAS*, 506, 5512  
 Gatto A., et al., 2016, *Monthly Notices of the Royal Astronomical Society*, 466  
 Gentry E. S., Krumholz M. R., Dekel A., Madau P., 2017, *MNRAS*, 465, 2471  
 Genzel R., et al., 2014, *ApJ*, 796, 7  
 Goetz M., Downes D., Greve A., McKeith C., 1990, *Astronomy and Astrophysics*, 240, 52  
 Gong H., Ostriker E., 2012, *The Astrophysical Journal Supplement Series*, 204  
 Greco J. P., Martini P., Thompson T. A., 2012, *ApJ*, 757, 24  
 Gronke M., Oh S. P., 2018, *MNRAS*, 480, L111  
 Gutcke T., Pakmor R., Naab T., Springel V., 2021, *Monthly Notices of the Royal Astronomical Society*, 501  
 Heckman T. M., Thompson T. A., 2017, *arXiv e-prints*, p. [arXiv:1701.09062](https://arxiv.org/abs/1701.09062)  
 Heckman T. M., Armus L., Miley G. K., 1990, *ApJS*, 74, 833  
 Heckman T. M., Lehnert M. D., Strickland D. K., Armus L., 2000, *ApJS*, 129, 493  
 Heckman T. M., Alexandroff R. M., Borthakur S., Overzier R., Leitherer C., 2015, *ApJ*, 809, 147  
 Heiderman A., Evans II N. J., Allen L. E., Huard T., Heyer M., 2010, *ApJ*, 723, 1019

- Hirose S., Hauschildt P., Minoshima T., Tomida K., Sano T., 2021, *Astronomy & Astrophysics*, 659
- Howard C., Pudritz R., Harris W., 2016, *Monthly Notices of the Royal Astronomical Society*, 461
- Hu C.-Y., Naab T., Glover S., Walch S., Clark P., 2017, *Monthly Notices of the Royal Astronomical Society*, 471
- Ichikawa T., Yanagisawa K., Itoh N., Tarusawa K., van Driel W., Ueno M., 1995, *The Astronomical Journal*, 109, 2038
- Jappsen A. K., Klessen R. S., Larson R. B., Li Y., Mac Low M. M., 2005, *A&A*, 435, 611
- Kaviraj S., et al., 2017, *MNRAS*, 467, 4739
- Keerthi Vasan G. C., et al., 2023, *ApJ*, 959, 124
- Kennicutt Jr. R. C., 1998, *The Astrophysical Journal*, 498, 541–552
- Kim J.-G., Kim W.-T., Ostriker E., 2018, *The Astrophysical Journal*, 859
- Krieger N., et al., 2021, *ApJ*, 915, L3
- Kroupa P., 2002, *Monthly Notices of the Royal Astronomical Society*, 322, 231
- Krumholz M. R., McKee C. F., Klein R. I., 2004, *ApJ*, 611, 399
- Leroy A., et al., 2015, *The Astrophysical Journal*, 814
- Levy R., et al., 2024, JWST Observations of Starbursts: Massive Star Clusters in the Central Starburst of M82, doi:10.48550/arXiv.2408.04135
- Li H., Vogelsberger M., Marinacci F., Gnedin O. Y., 2019, *Monthly Notices of the Royal Astronomical Society*, 487, 364
- Li X.-F., Zhu W., Wang T.-R., Feng L.-L., 2024, *arXiv e-prints*, p. arXiv:2410.09782
- Lim S., Hwang N., Lee M. G., 2013, *ApJ*, 766, 20
- Lynds C. R., Sandage A. R., 1963, *ApJ*, 137, 1005
- Mac Low M.-M., Ferrara A., 1999, *ApJ*, 513, 142
- MacFadyen A. I., Woosley S. E., 1999, *ApJ*, 524, 262
- Macciò A. V., Dutton A. A., van den Bosch F. C., Moore B., Potter D., Stadel J., 2007, *MNRAS*, 378, 55
- Maiolino R., et al., 2017, *Nature*, 544
- Martin C. L., 1999, *ApJ*, 513, 156
- Martin C. L., Shapley A. E., Coil A. L., Kornei K. A., Bundy K., Weiner B. J., Noeske K. G., Schiminovich D., 2012, *ApJ*, 760, 127
- Martini P., Leroy A., Mangum J., Bollato A., Keating K., Sandstrom K., Walter F., 2018, *The Astrophysical Journal*, 856
- Mayya Y., Carrasco L., Luna A., 2005, *The Astrophysical Journal*, 628
- Mayya Y. D., Bressan A., Carrasco L., Hernandez-Martinez L., 2006, *ApJ*, 649, 172
- McCarthy P. J., van Breugel W., Heckman T., 1987, *AJ*, 93, 264
- McCourt M., O’Leary R. M., Madigan A.-M., Quataert E., 2015, *MNRAS*, 449, 2
- McCraday N., Graham J. R., 2007, *ApJ*, 663, 844
- Melioli C., de Gouveia Dal Pino E. M., Geraissate F. G., 2013, *MNRAS*, 430, 3235
- Mitchell P. D., Schaye J., Bower R. G., Crain R. A., 2020, *MNRAS*, 494, 3971
- Miyamoto M., Nagai R., 1975, *Publications of the Astronomical Society of Japan*, 27, 533
- Murray N., Quataert E., Thompson T. A., 2005, *ApJ*, 618, 569
- Murray N., Quataert E., Thompson T., 2009, *The Astrophysical Journal*, 709
- Naab T., Ostriker J. P., 2017, *ARA&A*, 55, 59
- Naylor B., et al., 2010, *The Astrophysical Journal*, 722, 668
- Oehm W., Thies I., Kroupa P., 2017, *Monthly Notices of the Royal Astronomical Society*, 467
- Origlia L., Ranalli P., Comastri A., Maiolino R., 2004, *ApJ*, 606, 862
- Padoan P., Nordlund Å., 2011, *ApJ*, 730, 40
- Pandya V., et al., 2021, *MNRAS*, 508, 2979
- Paxton B., Bildsten L., Dotter A., Herwig F., Lesaffre P., Timmes a., 2010, *The Astrophysical Journal Supplement Series*, 192, 3
- Perrotta S., et al., 2023, *ApJ*, 949, 9
- Pillepich A., et al., 2018, *MNRAS*, 473, 4077
- Portinari L., Chiosi C., Bressan A., 1998, *Astronomy & Astrophysics - AS-TRON ASTROPHYS*, 334, 505
- Rahmati A., Pawlik A., Raičević M., Schaye J., 2012, *Monthly Notices of the Royal Astronomical Society*, 430
- Read J., Iorio G., Agertz O., Fraternali F., 2016, *Monthly Notices of the Royal Astronomical Society*, 462
- Rieke G. H., Loken K., Rieke M. J., Tamblyn P., 1993, *ApJ*, 412, 99
- Rodríguez-González A., Esquivel A., Velázquez P. F., Raga A. C., Melo V., 2008, *ApJ*, 689, 153
- Rupke D., 2018, *Galaxies*, 6, 138
- Rupke D. S., Veilleux S., Sanders D. B., 2005, *ApJS*, 160, 115
- Salak D., Nakai N., Miyamoto Y., Yamauchi A., Tsuru T. G., 2013, *PASJ*, 65, 66
- Sales L., Marinacci F., Springel V., Petkova M., 2013, *Monthly Notices of the Royal Astronomical Society*, 439
- Scannapieco E., Brüggén M., 2015, *ApJ*, 805, 158
- Schaller G., Schaerer D., Meynet G., Maeder A., 1992, *Astronomy and Astrophysics Supplement Series*, 96, 269
- Schaye J., et al., 2015, *MNRAS*, 446, 521
- Schneider E. E., Mao S. A., 2024, *ApJ*, 966, 37
- Schneider E. E., Ostriker E. C., Robertson B. E., Thompson T. A., 2020, *ApJ*, 895, 43
- Schreiber N., Genzel R., Lutz D., Kunze D., Sternberg A., 2001, *ApJ*, 552
- Schreiber N., Genzel R., Lutz D., Sternberg A., 2003, *The Astrophysical Journal*, 599
- Smith R., Flynn C., Candlish G., Fellhauer M., Gibson B., 2015, *Monthly Notices of the Royal Astronomical Society*, 448
- Smith B., et al., 2016, *Monthly Notices of the Royal Astronomical Society*, 466
- Somerville R. S., Davé R., 2015, *ARA&A*, 53, 51
- Stone J. M., Tomida K., White C. J., Felker K. G., 2020, *ApJS*, 249, 4
- Strickland D. K., Heckman T. M., 2009, *ApJ*, 697, 2030
- Strickland D., Stevens I., 2000, *Monthly Notices of the Royal Astronomical Society*, 314, 511
- Suchkov A. A., Balsara D. S., Heckman T. M., Leitherer C., 1994, *ApJ*, 430, 511
- Suchkov A. A., Berman V. G., Heckman T. M., Balsara D. S., 1996, *ApJ*, 463, 528
- Sukhbold T., Ertl T., Woosley S., Brown J., Janka H.-T., 2015, *The Astrophysical Journal*, 821
- Telesco C., Joy M., Dietz K., Decher R., Campins H., 1991, *The Astrophysical Journal*, 369
- Tenorio-Tagle G., Muñoz-Tuñón C., 1998, *MNRAS*, 293, 299
- Tenorio-Tagle G., Silich S., Muñoz-Tuñón C., 2003, *ApJ*, 597, 279
- Thompson T., Quataert E., Murray a., 2008, *The Astrophysical Journal*, 630, 167
- Thompson T., Quataert E., Zhang D., Weinberg D., 2015, *Monthly Notices of the Royal Astronomical Society*, 455, 1830
- Tomisaka K., Bregman J., 1993, *Publications- Astronomical Society of Japan*
- Tomisaka K., Ikeuchi S., 1988, *ApJ*, 330, 695
- Truelove K., Klein R., McKee C., Holliman J., Howell L., Greenough J., 1997, *Astrophysical Journal Letters* v.489, 489, L179
- Veilleux S., Cecil G., Bland-Hawthorn J., 2005, *ARA&A*, 43, 769
- Veilleux S., Maiolino R., Bolatto A. D., Aalto S., 2020, *A&ARv*, 28, 2
- Vink J., Sander A., 2021, *Monthly Notices of the Royal Astronomical Society*, 504
- Walter F., Weiss A., Scoville N., 2002, *ApJ*, 580, L21
- Wang P., Li Z.-Y., Abel T., Nakamura F., 2010, *ApJ*, 709, 27
- Weiner B. J., et al., 2009, *ApJ*, 692, 187
- Weldon A., et al., 2024, *MNRAS*, 531, 4560
- Westmoquette M., Smith L., Iii J., Walter F., 2012, *Monthly Notices of the Royal Astronomical Society*, 428
- Wild W., Harris A. I., Eckart A., Genzel R., Graf U. U., Jackson J. M., Russell A. P. G., Stutzki J., 1992, *A&A*, 265, 447
- Wills K., Das M., Pedlar A., Muxlow T., Robinson T., 2000, *Monthly Notices of the Royal Astronomical Society*, 316, 33
- Wolfire M., Hollenbach D., McKee C., Tielens A., Bakes E., 1995, *The Astrophysical Journal*, 443
- Woosley S. E., Weaver T. A., 1986, *ARA&A*, 24, 205
- Xu Y., Ouchi M., Nakajima K., Harikane Y., Isobe Y., Ono Y., Umeda H., Zhang Y., 2023a, *arXiv e-prints*, p. arXiv:2310.06614

- Xu X., Heckman T., Yoshida M., Henry A., Ohya Y., 2023b, *ApJ*, **956**, 142
- Yuan Y., Krumholz M. R., Martin C. L., 2023, *MNRAS*, **518**, 4084
- Yun M. S., 1999, in Barnes J. E., Sanders D. B., eds, IAU Symposium Vol. 186, *Galaxy Interactions at Low and High Redshift*. pp 81–
- Zhang D., 2018, *Galaxies*, **6**, 114

## APPENDIX A: DETAILS OF MASS MODEL

### A1 Stellar component

Observations in the 1970s and 1980s had identified M82 as a dusty disk galaxy with a central core. Later observations further revealed the existence of more complex structures. For instance, [Telesco et al. \(1991\)](#) identified characteristics of a bar in the central region of M82. The same structure was confirmed by [Wills et al. \(2000\)](#). In addition, some studies revealed the existence of spiral arms ([Mayya et al. 2005](#)) in M82. However, in this work, we omit the effect of bar and spiral arms, only account for a stellar fraction from a bulge, or in some contexts stellar spheroid ([Tomisaka & Bregman 1993](#); [Strickland & Stevens 2000](#)), and an exponential disk. The scale height and scale length of both the bulge and stellar disk have been constrained by several observations ([Ichikawa et al. 1995](#); [Schreiber et al. 2001](#); [Mayya et al. 2006](#)).

The work of [Levy et al. \(2024\)](#) and [Lim et al. \(2013\)](#) highlight a significant difference in the spatial distribution of stars formed in different starburst events in M82. The younger stars formed in the most recent starbursts we aim to simulate primarily concentrated in the nuclear region. In contrast, stars formed during earlier starbursts are dispersed more widely across the whole disk region, some of which reach as far as a few kpc. Based on the two-part SFH for stars located in the inner 3 kpc disk derived by [Mayya et al. \(2005\)](#), which consists of a continuous and moderate star formation lasted for over 10 Gyr with an SFR under  $0.3 M_{\odot} \cdot \text{yr}^{-1}$  and a brief starburst began around 0.8 Gyr ago and lasted for 0.3 Gyr with a peak SFR of  $20 M_{\odot} \cdot \text{yr}^{-1}$ , we estimate that around  $5.9 \times 10^9 M_{\odot}$  of stars were formed during this period, of which approximately  $3.3 \times 10^9 M_{\odot}$  of low to intermediate-mass stars remained till the beginning of the starburst we aim to simulate.

To describe the mass distribution and the potential of the stellar disk component, we use the widely adopted [Miyamoto & Nagai \(1975\)](#) disk profile. The density profile of a Miyamoto-Nagai disk is described by

$$\rho(R, z) = \frac{Mb^2[aR^2 + (a + 3\sqrt{z^2 + b^2})(a + \sqrt{z^2 + b^2})^2]}{4\pi[R^2 + (a + \sqrt{z^2 + b^2})^2]^{5/2}(z^2 + b^2)^{3/2}} \quad (\text{A1})$$

where  $M$  is the disk mass,  $a$  is the radial scale length, and  $b$  is the vertical scale height. The corresponding gravity potential is given by

$$\Phi(R, z) = \frac{-GM}{\sqrt{R^2 + (a + \sqrt{z^2 + b^2})^2}} \quad (\text{A2})$$

the mass of the stellar disk is set to the  $3.3 \times 10^9 M_{\odot}$  based on the above discussion, and the scale length and scale height of the stellar disk used in our simulation are  $1200 pc$  and  $200 pc$  respectively.

As for the bulge, the scale radius and mass of stellar bulge are  $r_0 = 450 pc$  and  $M_{\text{bulge}} = 6.0 \times 10^8 M_{\odot}$  respectively according to [Ichikawa et al. \(1995\)](#) and [Schreiber et al. \(2001\)](#). Previous studies often use the King profile to describe the mass distribution and potential of a bulge.

$$\rho(r) = \frac{\rho_0}{1 + (r/r_0)^3/2}, \quad (\text{A3})$$

where  $r_0$  is the scale radius of the stellar bulge. The potential of which is then

$$\Phi(r) = \frac{-GM_{\text{bulge}}}{r_0} \left[ \frac{\ln\{(r/r_0) + \sqrt{1 + (r/r_0)^2}\}}{r/r_0} \right]. \quad (\text{A4})$$

The bulge overlaps spatially with the recent starburst region. Therefore, a significant portion of the bulge's stellar mass likely originated from the recent starburst events we aim to simulate. Hence, unlike previous studies, we take a different approach in our simulation by incorporating the bulge as a part of the initial gas disk. By directly adding the mass of the bulge to the initial mass of the gas disk, we can obtain a gas disk profile that more accurately reflect the initial condition before the onset of the recent starburst. This method also allows for a more self-consistent formation of stars in the nuclear region during our starburst simulation. The detailed setup of the gas disk is described in the following section.

Note that, there are some uncertainties associated with the chosen parameters for both the bulge and stellar disk. These uncertainties arise from the notable extinction and assumptions on the stellar population, initial mass function, star formation history, etc. A more accurate understanding of the stellar component may be of considerable interest, but is beyond our ability.

### A2 Gas disk

Based on various observations, previous studies suggest that molecular gas is the dominant gas component in M82, followed by atomic hydrogen, and then warm and hot ionized gas. Currently, a considerable fraction of the molecular and atomic gas lies beyond the gaseous disc, due to the interaction with M81 and the outflow driven by the wind. Since our aim is to replicate the processes of starburst and outflow, and the interaction is relatively difficult to reproduce, we assume that most of the molecular and atomic gas belongs to the gaseous disk at the beginning of the simulation, i.e. about 20-50 Myr before the present epoch.

The mass of  $H_2$  in M82 is usually inferred from the observations of the CO line, where the CO- $H_2$  conversion factor,  $X_{\text{CO}}$ , has a noticeable uncertainty. The total mass of  $H_2$  in M82 at the present time varies from  $1.3 \times 10^9$  to  $2.4 \times 10^9 M_{\odot}$  in different studies, depending on the adopted value of  $X_{\text{CO}}$  ([Walter et al. 2002](#); [Salak et al. 2013](#); [Leroy et al. 2015](#); [Krieger et al. 2021](#)). Most of the  $H_2$  resides on the disk and streams. The molecular gas mass in the outflow comprises about 25% – 40% of the total molecular gas in M82. Meanwhile, the total mass of  $H_2$  mass in the nucleus region is around  $2.0 \times 10^8 M_{\odot}$  ([Wild et al. 1992](#); [Naylor et al. 2010](#)). In addition, [Leroy et al. \(2015\)](#) found a scale length of 0.6 kpc along the major axis and 0.5 kpc along the minor axis for the molecular gas in the disk of M82.

Observation conducted by [Crutcher et al. \(1978\)](#) suggested a total HI mass of around  $5.0 \times 10^8 M_{\odot}$  in M82. A similar result was obtained by [Appleton et al. \(1981\)](#), suggesting a total HI mass of  $7.2 \times 10^8 M_{\odot}$ . More recent observations indicate that the HI mass in M82 is between  $7.5$  and  $8.0 \times 10^8 M_{\odot}$  ([Yun 1999](#); [Chynoweth et al. 2008](#); [Blok et al. 2018](#)). [Leroy et al. \(2015\)](#) provides a detailed mapping of the HI distribution and found a scale length along the major axis to be 2.6 kpc.

In this work, we do not explicitly solve the chemistry of the gas component. Namely, we do not resolve the atomic, molecular, and ionized gas separately. Accounting for the uncertainties in the estimated mass of molecular gas and some of the gas in the nuclear region that had turned to stars in the past 20-50 Myr, we adopt a gas



**Table A1.** The parameters for the triple Miyamoto-Nagai disk model used in this work, where  $h$  is the scale height of the disk. Combining the three disk components results in a thick disk that corresponds to a radial density profile  $\rho \propto r^{-2}$  with ellipticity  $e=0.3$ .

Disk component	$b/h$	$a/h$	$m/m_{tot}$
1	1.0	2.39	1.37
2	1.0	2.67	0.0779
3	1.0	4.83	-0.449

disc with total mass  $M_{gd} \approx 2.5, 3.0, 3.5 \times 10^9 M_\odot$  respectively in different runs in our simulation.

Most of the previous simulational work of M82 uses a single Miyamoto & Nagai (1975) gas disk (e.g., Strickland & Stevens 2000; Cooper et al. 2008). More recently, Martini et al. (2018) proposed a different setup of the mass model to obtain the analytical form of the gravity potential. In their work, a triple Miyamoto-Nagai disk model (Smith et al. 2015) was employed. Though the Smith et al. (2015) model may produce an accurate fit to the mass distribution of an exponential gas disk, it fails to reproduce the gas profile of M82. Leroy et al. (2015) found the density profile of HI in M82 best fitted by a projected  $\rho \propto r^{-2}$  density profile, and H<sub>2</sub> best fitted by a projected  $\rho \propto r^{-3.5}$  density profile along the major axis. We employ a similar method to that described by Smith et al. (2015), using three Miyamoto-Nagai disks to fit the projected density profile found by Leroy et al. (2015). Our choice of parameters for the triple Miyamoto-Nagai disk model is given in Table A1.

### A3 Dark matter halo

Early research of the M82's rotational curve indicated that its rotational curve profile was likely to be Keplerian (Goetz et al. (1990)). Consequently, many previous simulations of M82 did not include the gravitational contribution from the dark matter halo. However, more recent observations of the CO line and star clusters suggest a different scenario. Greco et al. (2012) found the rotational curve of M82 is considerably flattened towards the outer region, which is commonly interpreted as evidence for the existence of the dark matter halo (DM halo hereafter). However, the complexity of interactions and mergers among the three members of the M81 group complicates efforts to accurately constrain the parameters of the DM halo. In Oehm et al. (2017), three-body simulation and Markov chain Monte Carlo (MCMC) method are employed to constrain the initial parameters of the three DM halos, and high-resolution N-body simulation was conducted to further investigate the evolution of the triplet. They demonstrated that the current DM halos, in which M82 and its neighboring galaxies are embedded, arise from distortion, blending, and merging of the original DM halos. Simple analytical models centered at M82 may struggle to reproduce the true profile of the galaxy's DM halo. For the sake of simplicity, we adopt a modified NFW profile in this work. The density distribution of the original NFW dark matter halo is given by

$$\rho(r) = \frac{\rho_0}{\frac{r}{R_s} \left(1 + \frac{r}{R_s}\right)^2}, \quad (\text{A5})$$

and the potential is given by

$$\Phi(r) = \frac{-4\pi G \rho_0 R_s^3}{r} \ln \left(1 + \frac{r}{R_s}\right). \quad (\text{A6})$$

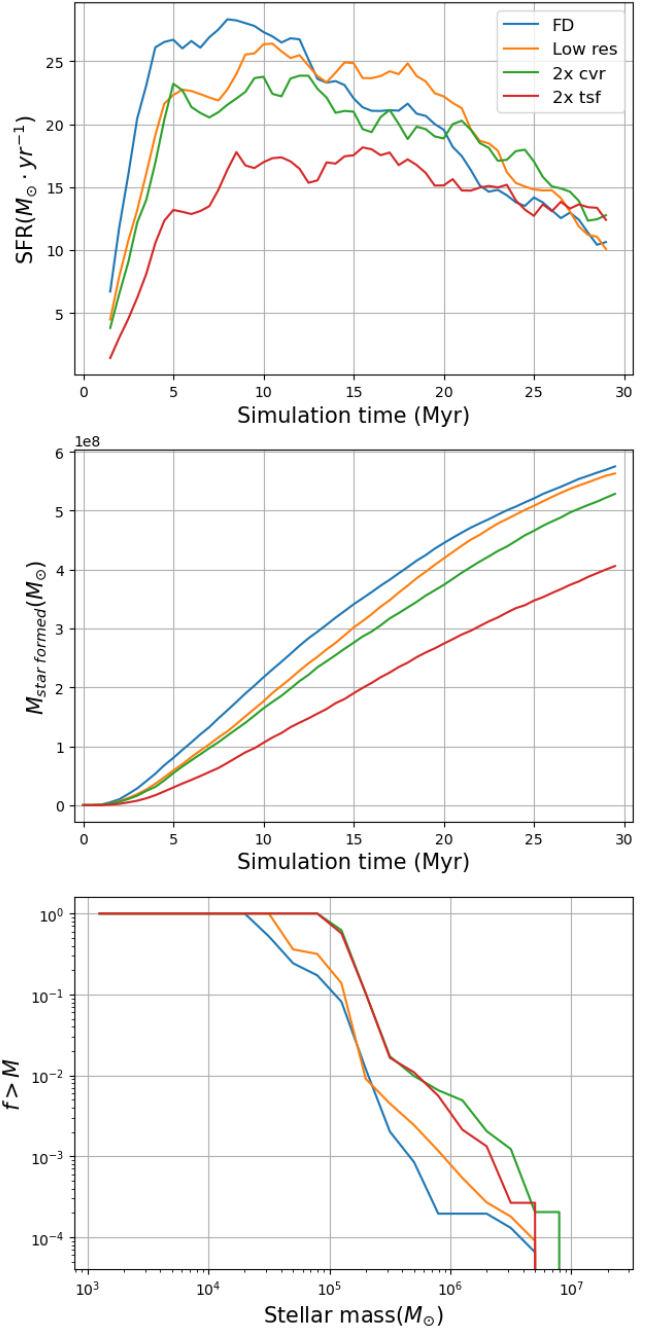


**Figure A1.** From the top to the bottom: star formation history, the integrated SFH, and the cumulative cluster mass function in simulation simulation FD, Low res, 2x cvr, and 2x tsf (see Table B1 for more details).

where  $R_s$  is the scale radius and  $\rho_0$  is the characteristic density, obeying the following relationships

$$R_s = R_{vir}/c, \quad (\text{A7})$$

where  $c$  is the concentration parameter.

Though the NFW profile has been widely adopted, it is not without its shortcomings, particularly in the scenario we are considering. The density of an NFW DM halo does not converge to a finite value towards the center, while observations suggest that many galaxies have a constant-density core in the center area of their DM halos. Such

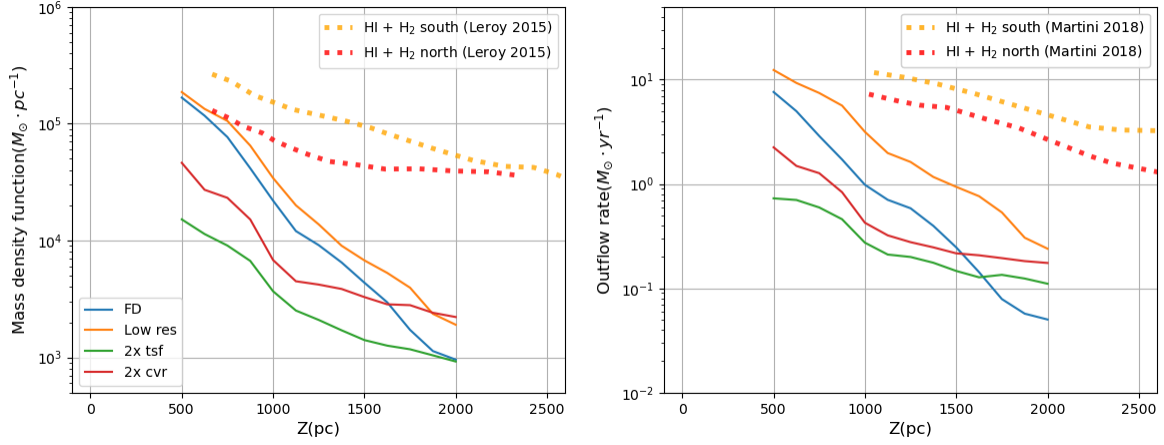


**Figure A2.** Same as Fig 14, the mass density function (left) and outflow rate at different heights (right) of the four simulations.

discrepancy is known as the cusp-core problem. Read et al. (2016) in their simulation shows that star formation and stellar feedback activities occurring in the embedded dwarf galaxy can transform the initial NFW DM halo into a ‘core-NFW’ profile with a constant density core in the starburst region ( $< R_{1/2}$ ) within a Hubble time. The profile of a ‘Core-NFW’ halo can be described by

$$M_{\text{cNFW}}(< r) = M_{\text{NFW}}(< r) \cdot f^n, \quad (\text{A8})$$

in which  $f = \tanh(\frac{r}{r_c})$ . In the case of M82, the galaxy has experienced multiple starburst events and developed a significant galactic scale outflow; a fully developed core-NFW profile is the adequate choice, which requires  $n = 1$ . The radius of the core  $r_c$  takes the radius of the inner starburst region, i.e.,  $r_c = 500 \text{ pc}$ . To further simplify the mass model and thus obtain an analytical expression of the potential, we used an NFW profile patch with a constant density core in the  $r < R_{1/2}$  region.

We have also adopted the  $c - M_{\text{vir}}$  relation proposed by Macciò et al. (2007) to further reduce the number of undetermined parameters of the DM halo, which states

$$\log c = 1.071 \pm 0.027 - (0.098 \pm 0.009)(\log M_{\text{vir}} - 12). \quad (\text{A9})$$

With the  $c - M_{\text{vir}}$  relation enforced, two free parameters remain:  $M_{\text{vir}}$  and  $R_{\text{vir}}$ . We used the Markov Chain Monte Carlo (MCMC) method to find the optimal combination of the two parameters that best fit the observed rotation curve of Greco et al. (2012). To obtain a more accurate result, we excluded the central 200 pc region, where the velocity dispersion is significantly higher than the local rotational velocity. Additionally, we also excluded the velocity bump located  $\sim 500 \text{ pc}$  at the eastern part of M82, which is caused by an SSC designated as cluster ‘z’ by McCrady & Graham (2007). We find the best fitting halo mass to be  $M_{\text{vir}} = 6.0 \times 10^{10} M_{\odot}$ , and the best fitting virial radius is  $R_{\text{vir}} = 53 \text{ kpc}$ . Fig 1 shows that the overall rotation curve of our model closely matches the observed result of Greco et al. (2012).

## APPENDIX B: CONVERGENCE TEST

To comprehensively assess our results, it is essential to examine the convergence of star formation-related recipes and modules across different resolutions. A key variable in the sink particle-based star formation recipe is the control volume radius, which influences both accretion and star formation rates. As resolution changes, the physical

**Table B1.** Simulations run for convergence test.  $R_{\text{cv}}$  indicates the radius of control volume for each sink particle, in unit of the grid size  $dx$ .

Simulation name	central resolution	$R_{\text{cv}}$	$t_{\text{sf}}$
Low res	8 pc	3.0 $dx$	$t_{\text{ff}}/0.2$
2x cvr	8 pc	6.0 $dx$	$t_{\text{ff}}/0.2$
2x tsf	8 pc	3.0 $dx$	$t_{\text{ff}}/0.1$

size of the control volume also changes. Additionally, the volume affected by feedback energy depends on the grid size. Therefore, different spatial resolutions can affect star formation and the impact of stellar feedback. Coarse simulations may not capture the free expansion phase of SN remnants, leading to the blending of SN ejecta with the ISM and lowering the core temperature to the thermally unstable regime ( $10^4 \sim 10^6 \text{ K}$ ). This can result in significant energy dissipation before expansion, artificially suppressing the effects of SNe.

To assess the impact of resolution and other parameters on our results, we conducted additional simulations with the setups listed in Table B1.

Figure A1 presents the SFH and stellar mass distribution for different resolutions and parameter variations. Lower resolution simulations exhibit a slower initial rise in SFR, reaching the peak SFR approximately 2 Myr later than the fiducial run. Despite this difference, the final total stellar mass remains similar to the fiducial run. Expanding the control volume slightly suppresses the SFR by 10 – 20% and reduces the total stellar mass by 10%. Meanwhile, increasing the star formation timescale significantly reduces the peak SFR by 40% and the total stellar mass by 30%. Additionally, the SFH profile for the longer star formation timescale shows a slower decline after the peak, suggesting potential for further star formation.

Altering the spatial resolution and control volume size has a modest impact on the SFH, resulting in approximately 10 – 20% variations. The overall profile of the SFH and the total stellar mass remain largely similar to the fiducial run, indicating that the SFH is relatively insensitive to these parameters. In contrast, adjusting the star formation timescale significantly reduces the SFR, leading to a flatter SFH profile. Therefore, accurately representing the star formation process within molecular clouds necessitates a careful choice of the star formation timescale.

The development of the outflow appears to be more sensitive to

changes in spatial resolution and control volume size than the SFH. The HI outflow rate in the low-resolution run exceeds that of the fiducial run by a factor of 1.5 at  $z = 500$  pc and by a factor of 4 at the edge of the simulation domain. Several factors may contribute to this discrepancy. First, lower resolution leads to SNe energy being injected into a larger volume, potentially resulting in greater radiative cooling losses during the free expansion phase but also more efficient acceleration of surrounding cool gas through direct energy injection. Second, lower resolution may limit the formation of unstable structures, preventing hot, ionized gas from escaping through gaps and channels between clumps, thus enhancing the efficiency of SN-driven outflows. Third, as shown in Section 4, the evolution of outflow rates is not synchronous in different simulations.

Expanding the control volume significantly reduces the cool gas outflow rate at  $z < 1600$  pc but increases it at  $z > 1700$  pc. This behavior arises from the time-dependent nature of the outflow rate at a given height  $z$ : it initially increases and then decreases due to the properties of the SFH and associated SN feedback. However, the timing of these increase and decrease phases can vary across simulations. A larger control volume reduces the SFR, leading to a lower peak outflow rate at all heights. Nevertheless, the outflow rate in the '2x cvr' simulation can exceed that of the FD simulation in certain regions and at specific times.

This paper has been typeset from a  $\text{\LaTeX}$  file prepared by the author.